NASA Technical Paper 2858

December 1988

A Spectral Collocation Solution to the Compressible Stability Eigenvalue Problem

Michéle G. Macaraeg,
Craig L. Streett,
and M. Y. Hussaini

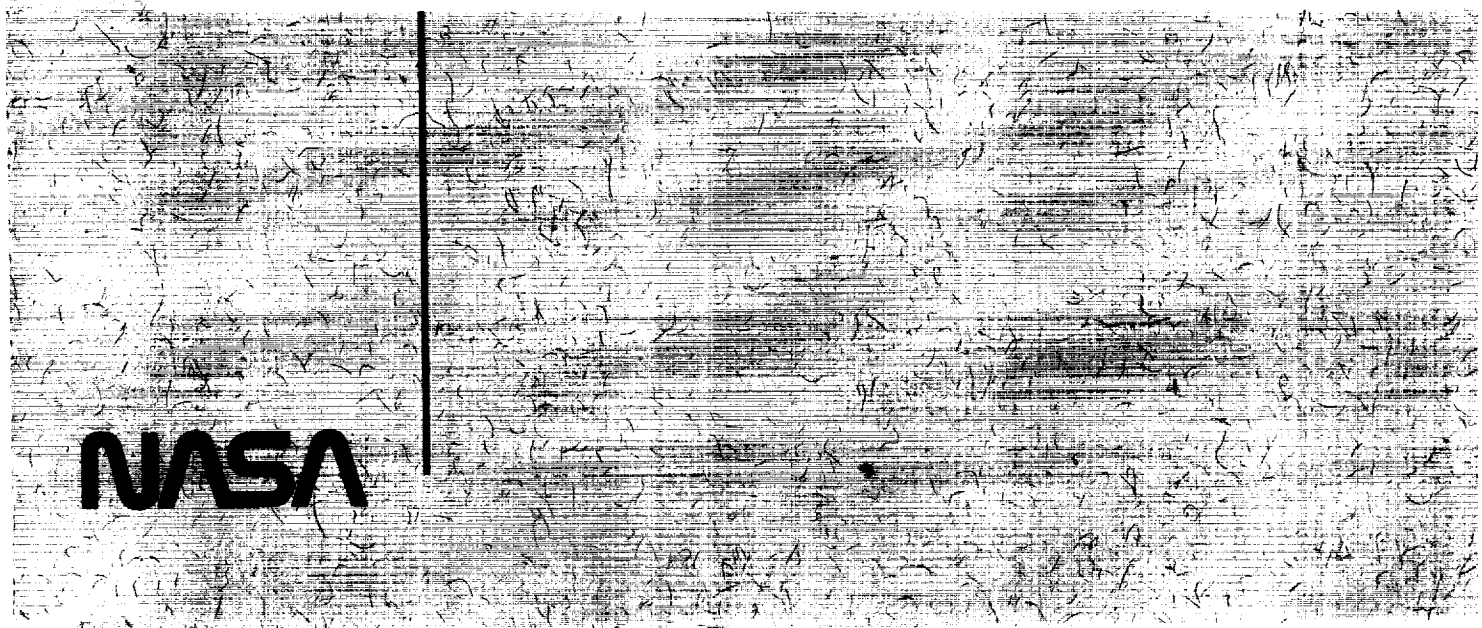

NASA

NASA Technical Paper 2858

1988

A Spectral Collocation Solution to the Compressible Stability Eigenvalue Problem

Michéle G. Macaraeg and Craig L. Streett
Langley Research Center
Hampton, Virginia

M. Y. Hussaini
Institute for Computer Applications in Scientific and Engineering (ICASE)
Langley Research Center
Hampton, Virginia

National Aeronautics and Space Administration

Scientific and Technical Information Division

Abstract

A newly developed spectral compressible linear stability code (SPECLS) using a staggered pressure mesh for analysis of shear flow stability is presented and applied to high-speed boundary layers and free shear flows. The formulation is the first application of a staggered mesh for a compressible flow analysis by a spectral technique. For equivalent accuracy of growth rates, an order of magnitude fewer points are needed by SPECLS than by a finite difference formulation. Supersonic disturbances, which are found to have highly oscillatory structures, have been resolved by a spectral multi-domain discretization, which requires a factor of three fewer points than the single-domain spectral stability code. The study indicates, as expected, that stability of mixing layers is enhanced by viscosity and increasing Mach number. The mean flow involves a jet being injected into a quiescent gas. Higher temperatures of the injected gas also enhance stability characteristics of the free shear layer.

Introduction

There is an enduring interest in the linear stability of shear flows. It can be attributed to the fact that currently this theory (used in conjunction with some semiempirical procedure such as an N-factor method) is virtually the only means of predicting the location of flow transition or indeed of determining whether a given laminar shear flow will become turbulent or not. At the present time, there is no prospect of a unified theory of transition even in low-speed flows (where some of the underlying mechanisms are relatively well-known), let alone in hypersonic flows. In view of the National Aero-Space Plane Project, the study of laminar-turbulent transition in supersonic and hypersonic flows has become extremely important.

As a short-term goal, it is imperative then to obtain linear stability results that account for factors such as body curvature, three-dimensional mean states, shocks, and real gas effects. The implicit assumption is that supersonic and hypersonic transition has its origin in linear instability and is not overly sensitive to details of the disturbance environment (not that Morkovin's bypasses (ref. 1), i.e., when flow transition occurs without any initial linear instabilities, are inapplicable to the hypersonic regime). Clearly, as Mack (ref. 2) points out, efficient, accurate, and robust linear stability codes are needed for use in a large number of design calculations.

This is the motivation behind the present work, which presents the first spectral compressible linear stability code (SPECLS) to solve the linearized Navier-Stokes equations. The newly developed pressure staggered mesh is shown to perform very well for spectral solutions to compressible flow problems. Spectral methods are known to yield highly accurate results using fewer grid points than finite difference formulations (refs. 3 and 4). In this study, results are presented to further substantiate this claim. In addition, a multi-domain spectral discretization in SPECLS (ref. 5) presented here deals economically with complex flows, which can include such features as multiple interior shear layers. The method is verified by comparison of results for boundary layers from an existing finite difference compressible linear stability code and by comparison with analytical results obtained for free shear flows.

Symbols

$\mathbf{A}$	matrix coefficients for second-derivative operators from equations (14) to (18)
$\mathbf{B}$	matrix coefficients for first-derivative operators from equations (14) to (18)
$\mathbf{C}$	matrix coefficients for zeroth-derivative operators from equations (14) to (18)
C_1, C_2, C_3	adjustable constants for grid stretching function, equations (21) and (22)
c_p^*	specific heat at constant pressure
$\mathbf{D}$	matrix coefficient for first-derivative operator premultiplied by ω
D	differentiation with respect to y
$\mathbf{E}$	matrix coefficient for zeroth-derivative operator premultiplied by ω
$\bar{\mathbf{e}}_{ij}^*$	dimensional viscous stress tensor defined in equation (5)
G	quantity that determines flow character, defined in equation (33)
$\mathbf{I}$	spectral interpolation operator
$\mathbf{L}$	spectral differentiation operator
M	Mach number
M_c	critical Mach number
p	mean flow pressure plus pressure perturbation
$\tilde{p}$	pressure perturbation

$\bar{p}^*$	time-dependent dimensional pressure
P_o	mean flow pressure
q^+	$= \alpha\tilde{u} + \beta\tilde{w}$
q^-	$= \alpha\tilde{w} + \beta\tilde{u}$
R^*	gas constant
Re	Reynolds number based on displacement thickness
t^*	dimensional time
T	mean flow temperature plus temperature perturbation
T_e	free-stream temperature; equivalent to T_1
T_o	mean flow temperature
T_1	free-stream temperature of injected gas
T_2	free-stream temperature of quiescent gas
u	streamwise mean flow plus perturbation velocity
$\tilde{u}$	streamwise complex disturbance of velocity
U_e	mainstream velocity
U_o	mean flow streamwise velocity
v	normal mean flow plus perturbation velocity
$\tilde{v}$	normal complex disturbance of velocity
V_o	mean flow normal velocity
w	spanwise mean flow plus perturbation velocity
$\tilde{w}$	spanwise complex disturbance of velocity
W_o	mean flow spanwise velocity
x	streamwise coordinate
y	normal coordinate
y_c	computational coordinate in the normal direction
$y_{\max}$	maximum extent of normal coordinate
y_p	normal coordinate in physical space
z	spanwise coordinate
α	disturbance wave number in the streamwise direction
β	disturbance wave number in the spanwise direction
β_T	ratio of quiescent gas to injected gas free-stream temperature, T_2/T_1
γ	ratio of specific heats
δ^*	displacement thickness of the velocity profile in the x-direction
θ	wave propagation angle of the disturbance
κ^*	coefficient of thermal conductivity
λ	second coefficient of viscosity
μ	dimensional coefficient of viscosity
ν_e	coefficient of kinematic viscosity
$\tilde{\rho}$	complex density disturbance
$\bar{\rho}^*$	time-dependent dimensional density
ρ_o	mean flow density
σ	Prandtl number
$\tilde{\tau}$	complex temperature disturbance
$\bar{\tau}_{ij}$	viscous stress tensor defined in equation (6)
ϕ	$= (\tilde{v},\ q^+,\ q^-,\ \tilde{\tau})^T$
ω	complex frequency
Subscripts:	
G	Gauss points
GL	Gauss-Lobatto points
i	imaginary part of
o	mean flow quantity
r	real part of
∞	free-stream quantity
Superscripts:	
G	Gauss points
GL	Gauss-Lobatto points
T	transpose
$*$	dimensional quantity
$'$	differentiation with respect to y
Acronyms:	
COSAL	compressible stability analysis code

MDSPD	multi-domain spectral discretization
SDSPD	single-domain spectral discretization
SPECLS	spectral compressible linear stability code

Basic Equations for Parallel Shear Flows

Mean Flow

The mean flows utilized in these studies are obtained from a spectral similarity solution for compressible shear flows. The basic spectral collocation technique is given in reference 6.

For the free shear flow analysis two gases are considered, with one of these gases taken as quiescent. The effect of relative temperature is studied by varying the parameter $\beta_T = T_2/T_1$, where T_2 refers to the free-stream temperature of the quiescent gas and T_1 the free-stream temperature of the injected gas. A typical mean flow streamwise velocity profile is given in figure 1.

Compressible Stability Equations

The basic equations governing the flow of a viscous compressible fluid are the Navier-Stokes equations. These equations in terms of a three-dimensional Cartesian coordinate system (x_1, x_2, x_3) for a heat-conducting perfect gas in dimensional form are

$$\frac{\partial \bar{u}_i^*}{\partial t^*} + \bar{u}_j^* \frac{\partial \bar{u}_i^*}{\partial x_j^*} = \frac{1}{\bar{\rho}^*} \frac{\partial \bar{\tau}_{ij}^*}{\partial x_j^*} \tag{1}$$

$$\frac{\partial \bar{\rho}^*}{\partial t^*} + \frac{\partial}{\partial x_j^*}\left(\bar{\rho}^* \bar{u}_j^*\right) = 0 \tag{2}$$

$$\bar{\rho}^* c_p^* \left(\frac{\partial \bar{T}^*}{\partial t^*} + \bar{u}_j^* \frac{\partial \bar{T}^*}{\partial x_j^*}\right) = \frac{\partial}{\partial x_j^*}\left(\bar{\kappa}^* \frac{\partial \bar{T}^*}{\partial x_j^*}\right) + \bar{\tau}_{ij}^* \bar{\mathbf{e}}_{ij}^* + \frac{\partial \bar{p}^*}{\partial t^*} + \frac{\partial}{\partial x_j^*}\left(\bar{u}_j^* \bar{p}^*\right) \tag{3}$$

$$\bar{p}^* = \bar{\rho}^* R^* \bar{T}^* \tag{4}$$

where u_i is the velocity in the coordinate direction x_i,

$$\bar{\mathbf{e}}_{ij}^* = \frac{1}{2}\left(\frac{\partial \bar{u}_i^*}{\partial x_j^*} + \frac{\partial \bar{u}_j^*}{\partial x_i^*}\right) \tag{5}$$

$$\bar{\tau}_{ij}^* = \bar{\mu}^* \bar{\mathbf{e}}_{ij}^* + \left(\bar{\lambda}^* \bar{\mathbf{e}}_{kk}^* - \bar{p}^*\right) \delta_{ij} \tag{6}$$

and i, j = 1,2,3 according to the summation convention. Asterisks denote dimensional quantities and overbars denote time-dependent quantities. In these equations $\bar{\kappa}^*$ is the coefficient of thermal conductivity; R^*, the gas constant; c_p^*, the specific heat at constant pressure (assumed constant); $\bar{\mu}^*$, the first coefficient of viscosity; $\bar{\lambda}^*$, the second coefficient of viscosity; and δ_{ij}, the Kronecker delta.

In this study, $x_i = (x, y, z)$ and $u_i = (u, v, w)$. All velocities are scaled by U_e, the mainstream velocity, and all lengths are scaled by δ^*, the displacement thickness of the velocity profile in the x-direction. The Reynolds number and Mach number are given by

$$\mathrm{Re} = \frac{U_e \delta^*}{\nu_e} \tag{7}$$

$$M = \frac{U_e}{\sqrt{\gamma R^* T_e}} \tag{8}$$

where ν_e and T_e are the kinematic viscosity and mean temperature in the free stream and γ is the ratio of specific heats. The Prandtl number σ is assumed to be 0.70 and $\bar{\mu}^*$ is evaluated by Sutherland's law.

If we assume that the base flow is a locally parallel boundary layer or free shear layer, then

$$u(x, y, z, t) = U_o(y) + \tilde{u}(y)\, e^{i(\alpha x + \beta z - \omega t)} \tag{9}$$

$$v(x,y,z,t) = \tilde{v}(y)\, e^{i(\alpha x+\beta z-\omega t)} \tag{10}$$

$$w(x,y,z,t) = W_o(y) + \tilde{w}(y)\, e^{i(\alpha x+\beta z-\omega t)} \tag{11}$$

$$p(x,y,z,t) = P_o(y) + \tilde{p}(y)\, e^{i(\alpha x+\beta z-\omega t)} \tag{12}$$

$$T(x,y,z,t) = T_o(y) + \tilde{\tau}(y)\, e^{i(\alpha x+\beta z-\omega t)} \tag{13}$$

where U_o, W_o, P_o, and T_o represent the steady unperturbed parallel shear layer (mean flow) properties; quantities with tildes ($\tilde{}$) denote complex disturbances; $V_o(y)$ is assumed zero since the flow is parallel; $P_o(y)$ is assumed constant across the shear layer; α and β are disturbance wave numbers in the x- and z-directions, respectively; and ω is the complex frequency. Equations (9) to (13) are substituted into equations (1) to (6), the mean flow terms are subtracted, and quadratic terms in the disturbances are neglected. The resulting system is the linearized compressible Navier-Stokes equations for the disturbance quantities given as follows (ref. 7):

$$\begin{aligned} &D^2(\alpha\tilde{u}+\beta\tilde{w}) + \frac{1}{\mu_o}\frac{d\mu_o}{dT_o}T_o' D(\alpha\tilde{u}+\beta\tilde{w}) + i\left(\frac{2\mu+\lambda}{\mu}-1\right)(\alpha^2+\beta^2)D\tilde{v} + \frac{1}{\mu_o}\frac{d\mu_o}{dT_o}(\alpha U_o'+\beta W_o')D\tilde{\tau} \\ &- \left[\frac{\mathrm{Re}}{\mu_o T_o}(\alpha U_o'+\beta W_o') - \frac{i}{\mu_o}\frac{d\mu_o}{dT_o}T_o'(\alpha^2+\beta^2)\right]\tilde{v} - \frac{i\mathrm{Re}}{\mu_o}(\alpha^2+\beta^2)\tilde{p} \\ &- \left[\frac{i\mathrm{Re}}{\mu_o T_o}(\alpha U_o+\beta W_o-\omega) + \frac{2\mu_o+\lambda}{\mu_o}\right](\alpha^2+\beta^2)(\alpha\tilde{u}+\beta\tilde{w}) \\ &+ \frac{1}{\mu_o}\left[\frac{d\mu_o}{dT_o}(\beta W_o'' + \alpha U_o'') + (\alpha U_o'+\beta W_o')T_o\frac{d^2\mu_o}{dT_o^2}\right]\tilde{\tau} = 0 \end{aligned} \tag{14}$$

$$\begin{aligned} &D^2\tilde{v} + i\left(1-\frac{\mu_o}{2\mu+\lambda}\right)D(\alpha\tilde{u}+\beta\tilde{w}) - \frac{\mu_o}{2\mu_o+\lambda} - \left[\frac{i\mathrm{Re}}{\mu_o T_o}(\alpha U_o+\beta W_o-\omega)+\alpha^2+\beta^2\right]\tilde{v} \\ &+ \frac{\mu_o'}{\mu_o}D\tilde{v} - \frac{\mathrm{Re}}{2\mu+\lambda}D\tilde{p} + i\left(\frac{1}{\mu_o}-\frac{2}{2\mu_o+\lambda}\right)\frac{d\mu_o}{dT_o}T_o'(\alpha\tilde{u}+\beta\tilde{w}) \\ &+ \frac{i}{(2\mu_o+\lambda)\mu_o}\frac{d\mu_o}{dT_o}(\alpha U_o'+\beta W_o')\tilde{\tau} = 0 \end{aligned} \tag{15}$$

$$D\tilde{v} + i(\alpha\tilde{u}+\beta\tilde{w}) - \frac{T_o'}{T_o}\tilde{v} + i\gamma M^2(\alpha U_o+\beta W_o-\omega)\tilde{p} - \frac{i}{T_o}(\alpha U_o+\beta W_o-\omega)\tilde{\tau} = 0 \tag{16}$$

$$D^2\tilde{\tau} + 2(\gamma-1)M^2\sigma\frac{\alpha V_o' + \beta W_o'}{\alpha^2+\beta^2}D(\alpha\tilde{u}+\beta\tilde{w}) + \frac{2T_o'}{\mu_o}\frac{d\mu_o}{dT_o}D\tilde{\tau} + 2(\gamma-1)M^2\sigma\frac{\alpha W_o' - \beta U_o'}{\alpha^2+\beta^2}D(\alpha\tilde{w}-\beta\tilde{u})$$
$$- \left[\frac{\mathrm{Re}}{\mu_o T_o}T_o' - 2i(\gamma-1)M^2\sigma(\alpha U_o' + \beta W_o')\right]\tilde{v} + \frac{i\mathrm{Re}\sigma}{\mu_o}(\gamma-1)M^2(\alpha U_o + \beta W_o - \omega)\tilde{p}$$
$$- \left[\frac{i\mathrm{Re}\sigma}{\mu_o T_o}(\alpha U_o + \beta W_o - \omega) + (\alpha^2+\beta^2) - (\gamma-1)\frac{\sigma M^2}{\mu_o}\frac{d\mu_o}{dT_o}\left(U_o'^2 + W_o'^2\right)\right.$$
$$\left. - \frac{1}{\mu_o}\frac{d^2\mu_o}{dT_o^2}T_o'^2 - \frac{1}{\mu_o}T_o''\frac{d\mu_o}{dT_o}\right]\tilde{\tau} = 0 \tag{17}$$

$$D^2(\alpha\tilde{w}-\beta\tilde{u}) + \frac{1}{\mu_o}\frac{d\mu_o}{dT_o}(\alpha W_o' - \beta U_o')D\tilde{\tau} + \frac{1}{\mu_o}\frac{d\mu_o}{dT_o}T_o'D(\alpha\tilde{w}-\beta\tilde{u}) - \frac{\mathrm{Re}}{\mu_o T_o}(\alpha W_o' - \beta U_o')\tilde{v}$$
$$+ \left[\frac{T_o'}{\mu_o}\frac{d^2\mu_o}{dT_o^2}(\alpha W_o' - \beta U_o') + \frac{1}{\mu_o}\frac{d\mu_o}{dT_o}(\alpha W_o'' - \beta U_o'')\right]\tilde{\tau}$$
$$- \left[\frac{i\mathrm{Re}}{\mu_o T_o}(\alpha U_o + \beta W_o - \omega) + (\alpha^2+\beta^2)\right](\alpha\tilde{w}-\beta\tilde{u}) = 0 \tag{18}$$

where primes and D indicate differentiation with respect to y. The equation of state is

$$\tilde{p} = \frac{\tilde{\rho}}{\rho_o} + \frac{\tilde{\tau}}{T_o} \tag{19}$$

where ρ_o is the mean flow density and $\tilde{\rho}$ the complex density disturbance. The boundary conditions are

$$\left.\begin{array}{ll} \tilde{v},\ \alpha\tilde{u}+\beta\tilde{w},\ \alpha\tilde{w}-\beta\tilde{u},\ \tilde{\tau}=0 & \left(\begin{array}{r} y=0,\ \text{Boundary layer} \\ y\to-\infty,\ \text{Free shear flow} \end{array}\right) \\ \tilde{v},\ \alpha\tilde{u}+\beta\tilde{w},\ \alpha\tilde{w}-\beta\tilde{u},\ \tilde{\tau}\to 0 & (y\to\infty) \end{array}\right\} \tag{20}$$

Solution Technique

Equations (14) to (18) and (20) constitute an eigenvalue problem for the complex frequency ω, once the disturbance wave numbers α and β are specified. Discretization of these equations in the y-direction forms a generalized matrix eigenvalue problem, suitable for computer solution. Equations (14) to (18) are essentially an eighth-order system; thus the eight boundary conditions (eqs. (20)) are sufficient for solution, and no boundary condition is applied to the disturbance pressure. Whatever discretization scheme is used must respect this arrangement, if a truly accurate solution is to be expected. Since stability analyses are inherently much more sensitive to inaccuracies than a large-scale aerodynamic calculation is, an artificial boundary condition could potentially impact stability results.

Staggered Discretization Scheme

The discretization scheme used here is a spectral collocation technique, using Chebyshev polynomials as basis functions. The nodes of the variables $\tilde{v}$, $q^+ = \alpha\tilde{u} + \beta\tilde{w}$, $q^- = \alpha\tilde{w} - \beta\tilde{u}$, and $\tilde{\tau}$ are located at the Gauss-Lobatto points (the extrema of the last Chebyshev polynomial retained in the expansion (ref. 4)); the energy and momentum equations are collocated at these points. Thus discrete boundary conditions may be imposed for these variables at both end points of the domain. The pressure nodes are located at the Gauss points (the zeros of

the first neglected polynomial) of a Chebyshev series one order less than that used for the other variables; the continuity equation is collocated at these points. Since no Gauss points fall on the boundary, we are free of any requirement of providing an artificial numerical boundary condition for pressure, and we have the proper balance of number of equations and unknowns.

The far-field boundary of the discretized domain is placed at a finite distance, typically $20\delta^*$ to $100\delta^*$ from the wall or shear-layer centerline. Extensive sensitivity studies were performed to determine the effect of this finite domain truncation.

Stretching is employed in the discretization to improve resolution near the wall and centerline. For the boundary layer, either of two stretching forms is used:

$$y_p = \frac{y_{\max}(C_2 - 1)^{C_1} y_c}{(C_2 - y_c^2)^{C_1}} \tag{21}$$

or

$$y_p = \frac{y_{\max} C_3 y_c}{1 + C_3 - y_c} \tag{22}$$

where y_p is the coordinate in the physical space $[0, y_{\max}]$, y_c is the computational coordinate ($y_c \in [0, 1]$, and C_1, C_2, and C_3 are adjustable constants. In equation (21) C_2 controls the amount of stretching and C_1 the rate. The smaller the quantity $(C_2 - 1)$, the stronger the stretching. In equation (22) C_3 controls both the rate and the amount of stretching. The smaller C_3, the stronger the stretching. In this work, C_1 is either 4 or 6 and C_2 ranges from 1.2 to 2.0; C_3 is used between 0.01 and 0.03. For the shear layer, equation (21) is used for stretching, yielding a physical space of $[-y_{\max}, y_{\max}]$ from $y_c \in [-1, 1]$.

Standard spectral collocation discretization formulas (refs. 3 and 4) are used to form matrix differentiation operators for both the Gauss-Lobatto ($\tilde{v}$, q^+, q^-, $\tilde{\tau}$) and the Gauss ($\tilde{p}$) grids, with the selected stretching function incorporated. Mean flow quantities from the spectral boundary layer code of reference 6 are spectrally interpolated onto the new mesh, and derivatives of these quantities obtained using the differentiation operators. The generalized matrix eigenvalue problem which results from this discretization is of the form

$$\begin{aligned}\mathbf{A}_{GL}\mathbf{L}_{GL}^2\boldsymbol{\phi} + \mathbf{B}_{GL}\mathbf{L}_{GL}\left(\boldsymbol{\phi} + \mathbf{I}_G^{GL}\mathbf{P}\right) \\ + \mathbf{C}_{GL}\left(\boldsymbol{\phi} + \mathbf{I}_G^{GL}\mathbf{P}\right) \\ = \omega\left[\mathbf{D}_{GL}\mathbf{L}_{GL}\left(\boldsymbol{\phi} + \mathbf{I}_G^{GL}\mathbf{P}\right)\right. \\ \left. + \mathbf{E}_{GL}\left(\boldsymbol{\phi} + \mathbf{I}_G^{GL}\mathbf{P}\right)\right]\end{aligned} \tag{23}$$

for the momentum and energy equations, and

$$\begin{aligned}\mathbf{B}_G\mathbf{L}_G\mathbf{I}_{GL}^G\boldsymbol{\phi} + \mathbf{C}_G\left(\mathbf{I}_{GL}^G\boldsymbol{\phi} + \mathbf{P}\right) \\ = \omega\mathbf{E}_G\left(\mathbf{I}_G^{GL}\boldsymbol{\phi} + \mathbf{P}\right)\end{aligned} \tag{24}$$

for the continuity equation, where **A**, **B**, **C**, **D**, and **E** are matrix coefficients derived from equations (14) to (18), **L** denotes a spectral differentiation operator, the unknown vector is $\boldsymbol{\phi} = [\tilde{v} \quad q^+ \quad q^- \quad \tilde{\tau}]^T$, and the vector **P** contains the disturbance pressure $\tilde{p}$. Subscripts GL and G denote location at or operation on Gauss-Lobatto and Gauss point grids, respectively; $\mathbf{I}_G^{GL}$ and $\mathbf{I}_{GL}^G$ are spectral interpolation matrices, from Gauss to Gauss-Lobatto points and vice versa.

The unknown vectors $\boldsymbol{\phi}$ and **P** are collected into a single vector, and the matrix equations (23) and (24) are assembled into a large generalized matrix eigenvalue problem for input into a standard library routine for solution. A complex modified QZ algorithm (ref. 8) is used to obtain the eigenvalues of the system directly; this is referred to as a global search. The most unstable eigenvalue is then selected and used as an input to an inverse Rayleigh method to purify the eigenvalue of the effects of roundoff error and to obtain the solution eigenvectors. In all cases, the global and local (Rayleigh-iterated) eigenvalues agreed to better than eight decimal places. No effort was made to optimize the standard routines used for these tasks; thus, no computation times are quoted or compared.

Spectral Multi-Domain Technique

The above discretization scheme is utilized in the spectral multi-domain technique developed by Macaraeg and Streett (ref. 5). This technique was formulated to handle both advection- and diffusion-dominated flow problems. Extremely large differences in discretization across an interface, through domain size, number of points, and stretchings, have been shown not to disrupt exponential-order accuracy (ref. 5). These advantages are crucial for solving problems with widely disparate scales, as is the case for flows undergoing transition or involving chemical reaction (ref. 9).

A simple one-dimensional, two-region example serves to illustrate the present method for interfacing two collocation-discretized regions. Consider the following second-order, potentially nonlinear boundary-value problem:

$$\left.\begin{array}{ll}[F(U)]_x - \nu U_{xx} = S(U) & x \in [-1, 1] \\ U(-1) = a & U(1) = b\end{array}\right\} \tag{25}$$

where F, S, and U are functions of x, and subscript x indicates differentiation with respect to x. We wish to place an interface at the point $x = m$ and have independent collocation discretizations in the regions $x^{(1)} \in [-1, m]$ and $x^{(2)} \in [m, 1]$. Even though the point $x = m$ is an interior point of the problem domain, simply applying a collocation statement there, utilizing a combination of the discretizations on either side, will not work; the resulting algebraic system is singular, because the spectral second-derivative operator has two zero eigenvalues; thus the patching together of two spectrally discretized domains yields potentially four zero eigenvalues in the overall algebraic system. Two of these eigenvalues are accounted for by imposition of boundary conditions, and one by continuity of the solution at the interface, but one zero eigenvalue remains in the system. To alleviate this difficulty, a global statement of flux balance is used. Rewriting equations (25) as

$$[G(U)]_x = S(U) \tag{26}$$

where the flux is

$$G(U) = F(U) - \nu U_x \tag{27}$$

and then integrating equation (26) from -1 to 1 results in

$$G(U)\Big|_{x=1} - G(U)\Big|_{x=-1} + [G]\Big|_{x=m} = \int_{-1}^{1} S(U)\,dx \tag{28}$$

If the jump in flux at the interface $[G]$ is zero, then equation (28) may be written

$$G(U)\Big|_{x=-1} \int_{-1}^{m} S(U)\,dx = G(U)\Big|_{x=1} - \int_{m}^{1} S(U)\,dx \tag{29}$$

The statement of global flux balance across the two regions, along with the assumption that the solution is continuous, provides the condition necessary to close the equation set which results from spectral discretization of equations (25) in two regions. Note that the left side of equation (29) involves the discretization in the region $x^{(1)} \in [-1, m]$, while the right side involves the region $x^{(2)} \in [m, 1]$. Since spectral collocation discretization strongly couples all points in their respective regions, equation (29) couples all points in both discretizations.

Note also that no statement is made concerning whether or not equations (25) are advection- or diffusion-dominated. Equations (25) are considered scalar equations here, although the above is extendable to a system.

A thorough treatment of the spectral multi-domain technique for compressible flow stability can be found in reference 10.

Verification

Boundary Layer

For verification, calculations were performed for the stability analysis of compressible two-dimensional similarity boundary layer profiles. A spectral mean flow code modified for compressible flow is used for this purpose (ref. 6). The cases to be presented are for $M_\infty = 0.00001$, 4.5, and 10, assuming adiabatic flow. Comparison with second-mode calculations by Mack (ref. 2) is also presented.

Initially a low Mach number, essentially incompressible case ($M_\infty = 0.00001$, $T_e = 520°\mathrm{R}$, $\mathrm{Re} = 2200$) is analyzed. A resolution study using SPECLS is shown in table I(a), which presents the eigenvalues versus number of grid points. A similar study is given for COSAL, a finite difference compressible stability code (ref. 7), in table I(b). Accuracy of the growth rate to 3 significant digits is obtained with 45 points in the spectral code; COSAL requires approximately 500 points for equivalent accuracy. It is of interest to note that converged values of growth rate differ in the third decimal place between the two codes. An independent calculation by L. M. Mack (Jet Propulsion Laboratory) agreed to four decimal places with SPECLS. Corresponding eigenfunctions for $\tilde{u}$ are given in figure 2 for both codes. The profiles are virtually identical.

A higher Mach number boundary layer profile perturbed by a three-dimensional disturbance is analyzed next. Conditions are $M_\infty = 4.5$, $T_e = 520°\mathrm{R}$, and $\mathrm{Re} = 10\,000$. A resolution study for the eigenvalue computations is given in table II for SPECLS and COSAL. Accuracy of growth rate to 3 significant digits is obtained with the spectral code using 81 points; in table II(b), COSAL requires approximately 800 points for equivalent accuracy. Eigenfunctions for $\tilde{u}$ are again shown for each code in figure 3. A multi-domain spectral discretization (MDSPD, ref. 5) in SPECLS with two domains requires one-third the number of points to obtain accuracy equivalent to that obtained with the single-domain spectral discretization (SDSPD), as illustrated in table III. The savings is significant considering that the number of operations in SPECLS varies as the cube of the number of points.

Insensitivity of these solutions to the locations of the far-field boundary is next illustrated with the MDSPD. The compressible case discussed above utilized an outer extent of $30\delta^*$. The same case was run with this far-field boundary distance halved and

doubled. Results are given in table IV. A factor-of-four change in outer extent basically does not change ω: the phase speed is constant to seven significant digits, and the growth rate is unchanged for five significant digits.

First and second mode eigenfunctions for $M_\infty = 10$, $T_e = 90°\mathrm{R}$, and $\mathrm{Re} = 100\,000$ are compared with compressible inviscid modes of neutral subsonic solutions (ref. 2). Plotted in figure 4 are the pressure eigenfunctions of the first mode from SPECLS and reference 2, respectively. The value of α is 1.844. Figure 5 displays similar plots for the second mode, with $\alpha = 4.9877$. Nondimensionalizations and properties differ for these comparison cases. Of relevance are the distinctive shapes of these $\tilde{p}$ modes; that is, the number of zeros in $\tilde{p}$ is one less than the mode number (ref. 2). The spectral code utilized 99 points for this case. A further comparison between Mack's calculations and SPECLS for equivalent flow properties and viscous flow at $M_\infty = 4.5$ and $T_e = 300°\mathrm{R}$ gave agreement to three significant figures in growth rate and five significant figures in phase speed.

Shear Layer

A further test of SPECLS is presented for a parallel shear flow. For verification, results are compared with those obtained by Blumen (ref. 11) for shear-layer instability of an inviscid compressible fluid.

The velocity profile whose stability is investigated is given in dimensionless form by

$$U_o = \tanh y \tag{30a}$$

$$W_o = 0 \tag{30b}$$

The basic thermodynamic state is assumed constant (ref. 11). Table V displays maximum growth rates determined by Blumen for a range of Mach numbers. The corresponding growth rates from SPECLS ($\mathrm{Re} = 10\,000$) are also displayed and were obtained using at most 81 collocation points. To determine the maximum growth rates using SPECLS, a plot of growth rate versus α is displayed in figure 6 for $M_\infty = 0.5$ and $M_\infty = 0.9$. The peaks occur at the growth rates given in table V for $M_\infty = 0.5$ and $M_\infty = 0.9$. Note in figure 6 that the lower Mach number flow is unstable to a larger range of wave numbers.

It is interesting to note the effect of Reynolds number on the maximum growth rate. Figure 7 displays a plot of α versus ω for $M_\infty = 0.9$ and $\mathrm{Re} = 100$. The maximum growth rate increases with increasing Reynolds number indicating that this shear-layer profile has an inviscid instability.

The real and imaginary parts of the eigenfunctions $\tilde{u}$, $\tilde{v}$, and $\tilde{p}$ for maximum growth rate are given in figure 8 for $M_\infty = 0.9$ and $\mathrm{Re} = 10\,000$. Each eigenfunction plot is normalized to one. Note that the real part of $\tilde{u}$ displays a small structure about the origin. This feature disappears as the neutral curve is approached, as illustrated in figure 9.

The manifestation of this structure is reflected in plots of magnitude and phase for $\tilde{u}$ as given in figures 10 and 11. Note the pronounced peak in the magnitude which decreases radically as the structure of $\tilde{u}$ about the inflection point disappears (fig. 10). As indicated in figure 11, the phase changes when the structure is prominent ($\alpha = 0.1$) from the smooth phase plot when the structure has disappeared ($\alpha = 0.4$). Viscosity appears to widen the appearance of this structure as exhibited in figure 12, which is a progression of $\tilde{u}$ plots for increasing α ($\mathrm{Re} = 100$).

A mean flow profile given by

$$U_o = 0.5(1 + \tanh y) \tag{31}$$

is also investigated (ref. 12) and verified with the incompressible result of reference 9. This growth rate should be multiplied by 2 to compare with the $\tanh y$ profile growth rate since the amplitude of equation (31) is one-half the value of equation (30a). The incompressible growth rate for this profile is also given in table V for comparison. Eigenfunction plots obtained from analyzing it are given in figure 13.

Sensitivity Analysis

When interpreting the results of a linear stability analysis, one must realize the sensitivity of these results to the accuracy of the mean flow with respect to the numerical scheme as well as properties assumed in the mean flow. To elucidate these points, we examine the sensitivity of calculated growth rates to the accuracy of the mean flow and assumed thermodynamic properties.

Consider a boundary layer flow with $M_\infty = 4.5$, $T_e = 300°\mathrm{R}$, $\lambda = (-2/3)\mu$, $\alpha = 0.6$, and $\beta = 1.0392$. This flow defines case 1 in table VI. (A lower T_e than in table II(a) is chosen to emphasize the extreme sensitivity of results to thermodynamic properties even at these relatively low temperatures.) A less than 3-percent change in the Prandtl number for this flow causes a 20-percent change in the calculated growth rate. Even more dramatic is the effect of changing the free-stream temperature (T_e) by 42 percent, which causes a 30-percent change in growth rate. A lesser effect, but nonetheless important for code validation purposes, is the effect of bulk viscosity illustrated by comparing case 4 with case 1. The effects of these properties are of course intensified at higher temperatures. Further points of interest are the effects of the numerical accuracy of the

mean flow, as well as the interpolation scheme employed to transfer mean flow values onto the SPECLS grid. These latter effects, although minimal, cumulatively cause a difference in the second significant figure of the growth rate relative to case 1.

Also relevant is the effect of Prandtl number on the generalized inflection points (defined by $(U_o'/T_o)' = 0$) for shear flows, since these flows are characterized by inflectional instabilities. For demonstration, we compare plots of $(U_o'/T_o)'$ versus y in figure 14 corresponding to two shear-layer mean flows with $M_\infty = 5$ and $\beta_T = 0.6$. The solid line represents a mean flow with $\sigma = 0.7$ and Sutherland-law viscosity, representative of a typical profile in the present report. The dashed curve is for $\sigma = 1$ and $\mu = T$, representative of a profile from reference 13. Note that the number and locations of inflection points in these two cases are vastly different, which has important implications for studies involving overly simplified constitutive relations. Multiple inflection points are found not to occur for as high a Mach number as 10 assuming the more realistic constitutive relations.

Stability of a Compressible Shear Layer

The spectral stability code is now used to analyze the stability of a compressible shear layer. This mean flow is a spectral collocation similarity solution for free shear flows and is studied to understand the impact of transition on fuel-air mixing efficiency in scramjet combustors. It has been observed experimentally that the mixing efficiency is decreased fourfold in the range from Mach 1 to 4 (refs. 14 and 15). The cause of this trend is unknown. However, it is well-known that turbulent mixing is many orders of magnitude faster than laminar. Ideally one would like to be able to manipulate the downstream evolution of shear layers to enhance mixing. The initial stages of shear-flow instabilities are driven by linear mechanisms. Understanding the growth and propagation of the disturbance in these early stages not only would allow a better understanding of the onset of transition but also would allow initiation of the transition process in a numerical model so that the physics might be systematically studied. This study investigates a range of Mach numbers, gas temperatures, and disturbance wave numbers. Unless otherwise stated, Re = 10 000. The mean flow in all cases involves a jet being injected into a quiescent gas.

Effect of Mach Number and Temperature on Stability

For the cases under study, lower Mach numbers correspond to a more unstable mean flow than higher Mach numbers do. This point is illustrated in figure 15, which displays growth rate versus α for a range of Mach numbers. The wave propagation angle θ is defined as

$$\theta = \cos^{-1} \frac{\alpha}{(\alpha^2 + \beta^2)^{1/2}} \tag{32}$$

The value of this angle is chosen to be 60° since disturbances that are propagated at an angle of 50° to 60° relative to the direction of flow are known (ref. 9) to experience the greatest amplification. As can be seen in figure 15, the lower the Mach number, the wider the band of wave numbers that can cause the flow to become unstable.

The stability characteristics of the shear flow are also quite sensitive to the temperature difference between the injected and the quiescent gas. Figure 16 illustrates this sensitivity. The plot displays growth rate versus α for a wave propagation angle of 60° and Mach 3 flow. The three temperature cases given in the plot are cold injection (500°R) into a hot quiescent gas (2500°R), $\beta_T = 5$; cold injection into a cold gas (500°R), $\beta_T = 1$; and hot injection (2500°R) into a cold quiescent gas (500°R), $\beta_T = 0.2$. The condition relevant to the scramjet is $\beta_T = 5$, since in this context a cold fuel is injected into a much hotter airstream (ref. 16). Mixing efficiency is greatly enhanced by transition, so the greater instability of the shear layer at this temperature is a favorable scenario for increased fuel-air mixing. Cold injection into a cold quiescent gas is less unstable, and hot injection into a cold gas is the most stable of these cases. It seems that if the fuel temperature increases relative to the airstream, its stability is enhanced. This observation has important implications. For example, cooling an aircraft by running fuel under the skin hinders mixing efficiency since heating the injected fuel decreases the range of wave numbers that can induce an instability necessary for flow transition. The impact of temperature differential on stability results depends heavily on the assumed temperature profiles. Contrasting the above effects of temperature on stability with previous work (ref. 13) reveals discrepancies because of overly simplified temperature profiles and constitutive relations assumed in these earlier studies.

Effect of Mach Number, Temperature, and Wave Number on Disturbance Structure

Three-dimensional modes. It is not surprising that distinct differences in the shapes of temperature disturbance eigenfunctions occur as the gas temperatures are varied. To illustrate this point, figure 17 displays temperature disturbance eigenfunctions of

mean flows which differ only in the temperature of the injected gas with respect to the quiescent gas. The Mach number of the injected gas is 2 and $\theta = 60°$, with $\alpha = 0.0862$ and $\beta = 0.1493$. The qualitative differences essentially reflect the effects of viscosity which varies because of the different temperature distributions for each case.

Further, the disturbance eigenfunctions significantly tighten in structure as α increases; thus greater resolution is required for the SDSPD. A progression of eigenfunction plots for increasing α ($\theta = 60°$) is given in figures 18 and 19.

Difficulties in resolution similarly occur for higher Mach number disturbances. The SDSPD in SPECLS had difficulty resolving eigenfunctions beyond $M_\infty = 3.75$ for $\beta_T = 5$ and as early as $M_\infty = 3$ for $\beta_T = 0.2$. Restrictions on the allowable stretching for single-domain spectral methods contribute to this difficulty. The MDSPD in SPECLS is especially useful in these cases. Examples of its usage for cases requiring very severe stretchings are given later.

To illustrate the effect of increasing Mach number on the three temperature cases of figure 16, plots of pressure disturbances are given in figure 20. The wave propagation angle is 60°, and the disturbances correspond to comparable growth rates (approximately 10^{-2}) in each case. Note that for $\beta_T = 0.2$ (fig. 20), an additional lobe develops at $M_\infty = 3$. Beyond $M_\infty = 3$ the single-domain code has difficulties resolving disturbance eigenfunctions. Contrast figure 20(a) with figure 20(b), for $\beta_T = 5$. The $\tilde{p}$ eigenfunctions maintain a single lobe and are one-signed. Cases are resolved up to $M_\infty = 3.75$ (note that the spatial scale is for the interval $[-10, 10]$, though the actual extent is $[-100, 100]$). Similarly, the structure at $\beta_T = 1$ (fig. 20(c)) is resolvable to $M_\infty = 3.75$ although the real part of $\tilde{p}$ differs from the preceding case.

Two-dimensional modes. The above studies involve three-dimensional disturbances with a wave propagation angle of 60°. Preliminary results indicate that two-dimensional disturbances ($\beta = 0$) exhibit similar trends; however, difficulties in resolving eigenfunctions with the SDSPD occur at lower Mach numbers. Again at higher α, disturbance eigenfunctions tighten radically beyond the limit at which a single-domain spectral method can resolve, and cases become harder to resolve as β_T decreases (cooling). This observation is demonstrated in figure 21, which plots a sequence of $\tilde{p}$ and $\tilde{\tau}$ eigenfunctions for increasing α. The mean flow corresponds to $M_\infty = 1$ and Re = 10 000 with $\beta_T = 0.2$. Note the extremely tight structures in $\tilde{p}$ and $\tilde{\tau}$ as α increases. Again note that while $\tilde{\tau}$ is plotted on the interval $[-10, 10]$, the actual spatial extent is $[-100, 100]$. Numerical oscillations in $\tilde{p}$ for $\alpha = 5$ and 6 are quite pronounced, indicating breakdown of resolution.

A MDSPD is ideal for flows with radical scale differences (ref. 9). To illustrate this point, $\tilde{p}$ and $\tilde{v}$ eigenfunctions obtained from a multi-domain discretization are displayed in figure 22 for Re = 10 000 and $\alpha = 5$, the case discussed previously. Adjacent to the MDSPD results are the SDSPD solutions for $\tilde{p}$ and $\tilde{v}$. The multi-domain solution remains oscillation free. The number of points in each discretization is roughly 100; however, the multi-domain solution utilizes three domains, with 41 points in the center domain between -0.5 and 0.5, 25 points in the left domain between -100 and -0.5, and 37 points in the right domain between 0.5 and 100. The plot of the pressure disturbance for the entire spatial extent $[-100, 100]$ as obtained from the multi-domain solution is given in figure 23, to illustrate the fineness of the structure which is resolved.

The preceding case ($\alpha = 5$) is found to be resolvable by the SDSPD, but only after considerable trial and error stretching of the mesh for a variety of resolutions. The important point is that the MDSPD is quite robust and gives accurate eigenvalues over a wide range of stretching parameters. This observation is illustrated in table VII, which lists a range of stretching parameters and corresponding phase speeds and growth rates again for $M_\infty = 1$, Re = 10 000, $\beta_T = 0.2$, and $\alpha = 5$. Both the SDSPD and the MDSPD for this illustration utilized 99 points with the same outer extent. Note that for the SPSPD cases changing the stretching parameter by approximately 25 percent causes about a 10-percent change in phase speed and over a 50-percent change in growth rate. Contrast this sensitivity with the MDSPD. The stretching parameter is allowed to vary 100 percent in the center domain (three domains are utilized with interfaces at ± 1). The phase speed has changed by less than 1 percent and the growth rate by only 6 percent. This robustness is extremely important since one usually has no idea of the value of the phase speed or growth rate. In addition, one needs to determine whether the disturbance mode is spurious—by measuring its persistence over a wide range of resolutions.

Supersonic Disturbances

As mentioned earlier, the disturbance eigenfunctions become increasingly complex as Mach number is increased. These higher Mach number cases are unresolvable by the SDSPD. To illustrate, a series

of $\tilde{p}$ and $\tilde{v}$ eigenfunctions calculated by the SDSPD stability code are displayed in figures 24 and 25, respectively, for a disturbance wave angle of 60°. Note that at $M_\infty = 3.5$ the injected gas side of the disturbance begins to take on an oscillatory nature; at $M_\infty = 3.75$ these oscillations are more pronounced. It is well-known that for supersonic disturbances the eigenfunction structure is oscillatory (ref. 12). (A supersonic disturbance occurs when the wave velocity of the disturbance relative to the local flow, in the direction of wave propagation, has a magnitude greater than the speed of sound.) The MDSPD is able to capture the structure of these supersonic modes with relative ease. Figure 26 displays two unstable supersonic modes that are associated with the instability of a Mach 4, $\beta_T = 1$, free shear flow. The disturbance wave numbers are $\alpha = 0.30416$ and $\beta = 0.2017$. The MDSPD involves three domains: 105 points on the oscillatory side, 41 points in the inner domain, and 25 points in the outer domain where the profile is smooth. Interface locations are ± 1. Note further the level of complexity of the $\tilde{\tau}$ eigenfunctions of this case. Figure 27 is a plot of $\tilde{\tau}$ for both modes on a full scale from 100 to -100 and a greatly expanded scale from 10 to -10. The center structure is an added complexity which also requires adequate resolution and further illustrates the necessity of a flexible discretization scheme like a MDSPD.

The Mach number at which no unstable subsonic modes exist (i.e., all unstable modes are supersonic) is called the critical Mach number (M_c). Figure 28 displays a plot of M_c versus β_T for both two- and three-dimensional ($\theta = 60°$) disturbances. It is found that M_c for a three-dimensional disturbance at a given β_T is equal to the two-dimensional M_c multiplied by the reciprocal of the cosine of the propagation angle of the three-dimensional mode.

An analysis from inviscid theory of compressible shear flows substantiates this relationship. A quantity G, defined as follows (ref. 13), determines the character of the flow:

$$G = \frac{\beta_T}{\cos^2\theta} - M^2\left(U_o - \frac{\omega}{\alpha}\right)^2 \tag{33}$$

It can be shown (ref. 13) that the point where modes appear supersonic occurs at $G = 0$. We solve for M using this condition:

$$M = \frac{\beta_T \cos\theta}{U_o - \frac{\omega}{\alpha}} \tag{34}$$

For a two-dimensional mode $\theta = 0$, so that

$$M = \frac{\beta_T}{U_o - \left(\frac{\omega}{\alpha}\right)_{2D}}$$

The first occurrence of this relationship is the critical Mach number. Therefore, for a given mean flow the following is true:

$$\frac{(M_c)_{3D}}{(M_c)_{2D}} = \frac{\frac{\cos\theta}{U_o - (\omega/\alpha)_{3D}}}{\frac{1}{U_o - (\omega/\alpha)_{2D}}} \tag{35}$$

It was found that at the critical Mach number for a given mean flow

$$\left(\frac{\omega}{\alpha}\right)_{3D} \approx \left(\frac{\omega}{\alpha}\right)_{2D} \tag{36}$$

so that

$$(M_c)_{3D} = (M_c)_{2D}\,(\cos\theta) \tag{37}$$

Conclusions

The first spectral collocation linear stability code for compressible flow (SPECLS) is presented. The accurate discretization (staggered pressure grid) can be employed in nonlinear simulations. Verification cases for high-speed boundary layers indicate an order-of-magnitude reduction in the number of points required to obtain equivalent accuracy in growth rates with a finite difference formulation. In addition, a multi-domain spectral discretization (MDSPD) in SPECLS is found to require a factor of three fewer points, which is significant since the operation count of the spectral formulation varies as the cube of the number of points. The highly irregular structures of the supersonic modes are easily resolved by a MDSPD, which is shown to be highly robust over a wide range of stretching parameters and resolutions.

The stability analysis of a compressible shear flow is presented. The study indicates that for subsonic disturbances stability of mixing layers is enhanced by viscosity, increasing Mach number, and higher temperatures of the injected gas. The critical Mach number for three-dimensional disturbances is shown to be higher than for two-dimensional modes, the proportionality constant being the inverse of the cosine of the propagation angle. The exact value of this Mach number depends on the differential temperature between the two gases: The lower the value of β_T, the lower the Mach number at which supersonic modes appear.

Acknowledgments

The authors are deeply appreciative of the assistance of L. M. Mack, Jet Propulsion Laboratory, during the verification stages of SPECLS.

NASA Langley Research Center
Hampton, VA 23665-5225
October 21, 1988

References

1. Morkovin, Mark V.: *Transition at Hypersonic Speeds.* NASA CR-178315, 1987.
2. Mack, L. M.: *Boundary Layer Stability Theory.* NASA CR-131501, 1969.
3. Hussaini, M. Yousuff; Streett, Craig L.; and Zang, Thomas A.: Spectral Methods for Partial Differential Equations. *Transactions of the First Army Conference on Applied Mathematics and Computing,* ARO Rep. 84-1, U.S. Army, Feb. 1984, pp. 883–925. (Available from DTIC as AD P002 980.)
4. Streett, C. L.: Spectral Methods and Their Implementation to Solution of Aerodynamic and Fluid Mechanic Problems. *Int. J. Numer. Methods Fluids,* vol. 7, no. 11, Nov. 1987, pp. 1159–1189.
5. Macaraeg, Michéle G.; and Streett, Craig L.: Improvements in Spectral Collocation Discretization Through a Multiple Domain Technique. *Appl. Numer. Math.,* vol. 2, no. 2, Apr. 1986, pp. 95–108.
6. Streett, C. L.; Zang, T. A.; and Hussaini, M. Y.: Spectral Methods for Solution of the Boundary-Layer Equations. AIAA-84-0170, Jan. 1984.
7. Malik, Mujeeb R.; and Orszag, Steven A.: Linear Stability Analysis of Three-Dimensional Compressible Boundary Layers. *J. Sci. Comput.,* vol. 2, no. 1, Mar. 1987, pp. 77–97.
8. Wilkinson, J. H.: *The Algebraic Eigenvalue Problem.* Oxford Univ. Press, c.1965.
9. Macaraeg, Michéle G.; and Streett, Craig L.: A Spectral Multi-Domain Technique for Analysis of Chemically Reacting Flows. *Numerical Methods in Laminar and Turbulent Flow, Volume 5, Part 2,* C. Taylor, W. G. Habashi, and M. M. Hafez, eds., Pineridge Press (Swansea, U.K.), 1987, pp. 2029–2037.
10. Macaraeg, Michéle G.; Streett, Craig L.; and Hussaini, M. Yousuff: A Spectral Multi-Domain Technique Applied to High-Speed Chemically Reacting Flows. NASA paper presented at the Second International Symposium on Domain Decomposition Methods (Los Angeles, California), Jan. 14–16, 1988.
11. Blumen, William: Shear Layer Instability of an Inviscid Compressible Fluid. *J. Fluid Mech.,* vol. 40, pt. 4, Mar. 9, 1970, pp. 769–781.
12. Michalke, A.: On the Inviscid Instability of the Hyperbolic-Tangent Velocity Profile. *J. Fluid Mech.,* vol. 19, pt. 4, Aug. 1964, pp. 543–556.
13. Gropengiesser, Hans: *Study on the Stability of Boundary Layers and Compressible Fluids.* NASA TT F-12786, 1970.
14. Papamoschou, D.; and Roshko, A.: Observations of Supersonic Free Shear Layers. AIAA-86-0162, Jan. 1986.
15. Brown, Garry L.; and Roshko, Anatol: On Density Effects and Large Structure in Turbulent Mixing Layers. *J. Fluid Mech.,* vol. 64, pt. 4, July 24, 1974, pp. 775–816.
16. Drummond, J. Philip: A Two-Dimensional Numerical Simulation of a Supersonic, Chemically Reacting Mixing Layer. NASA TM-4055, 1988.

Table I. Temporal Eigenvalues for Low Mach Number, Incompressible Case

$[M_\infty = 0.00001,\ T_e = 520°\text{R},\ \text{Re} = 2200,\ \alpha = 0.2,\ \beta = 0]$

(a) Calculated With SPECLS (SDSPD)

Number of points	ω_r	ω_i
35	$5.972895550 \times 10^{-2}$	$4.163678340 \times 10^{-3}$
39	$5.982453898 \times 10^{-2}$	$4.051750872 \times 10^{-3}$
41	$5.984158831 \times 10^{-2}$	$4.016799466 \times 10^{-3}$
45	$5.983655920 \times 10^{-2}$	$4.022189152 \times 10^{-3}$
65	$5.983575125 \times 10^{-2}$	$4.023290767 \times 10^{-3}$
95	$5.983575084 \times 10^{-2}$	$4.023291203 \times 10^{-3}$
200	$5.983575084 \times 10^{-2}$	$4.023291203 \times 10^{-3}$

(b) Calculated With COSAL

Number of points	ω_r	ω_i
100	$5.983647688 \times 10^{-2}$	$3.96449684 \times 10^{-3}$
200	$5.981935522 \times 10^{-2}$	$4.004225579 \times 10^{-3}$
300	$5.981623402 \times 10^{-2}$	$4.01151043 \times 10^{-3}$
500	$5.981464629 \times 10^{-2}$	$4.015224481 \times 10^{-3}$
1025	$5.981396790 \times 10^{-2}$	$4.016810997 \times 10^{-3}$
1200[a]	$5.981375400 \times 10^{-2}$	$4.017305399 \times 10^{-3}$

[a]With Richardson extrapolation.

Table II. Temporal Eigenvalues for Higher Mach Number Case

$[M_\infty = 4.5,\ T_e = 520°\text{R},\ \text{Re} = 10\,000,\ \alpha = 0.6,\ \beta = 1.0392]$

(a) Calculated With SPECLS (SDSPD)

Number of points	ω_r	ω_i
45	0.49578803	$4.36603960 \times 10^{-3}$
51	.49591572	$3.749838454 \times 10^{-3}$
65	.496217679	$3.727396074 \times 10^{-3}$
81	.496093364	$3.761833505 \times 10^{-3}$
95	.496106105	$3.763494422 \times 10^{-3}$
120	.496104826	$3.764796852 \times 10^{-3}$
151	.496104845	$3.764820857 \times 10^{-3}$
200	.496104846	$3.764820881 \times 10^{-3}$

(b) Calculated With COSAL

Number of points	ω_r	ω_i
211	0.496035465	$3.720663427 \times 10^{-3}$
513	.495990048	$3.688194736 \times 10^{-3}$
813	.495984488	$3.684224749 \times 10^{-3}$
1025	.495983122	$3.683247436 \times 10^{-3}$
1500	.495981891	$3.682367822 \times 10^{-3}$
1500[a]	.495980770	$3.681512173 \times 10^{-3}$

[a] With Richardson extrapolation.

Table III. Temporal Eigenvalues Calculated With MDSPD in SPECLS

$[M_\infty = 4.5,\ T_e = 520°\text{R},\ \text{Re} = 10\,000,\ \alpha = 0.6,\ \beta = 1.0392]$

Number of points				
First domain	Second domain	Total	ω_r	ω_i
25	17	42	0.496102327	$3.764737236 \times 10^{-3}$
31	25	56	.496104982	$3.764889142 \times 10^{-3}$
37	25	62	.496104984	$3.764890672 \times 10^{-3}$

Table IV. Effect of Far-Field Boundary Location on Temporal Eigenvalues Calculated With MDSPD in SPECLS

$[M_\infty = 4.5,\ T_e = 520°\text{R},\ \text{Re} = 10\,000,\ \alpha = 0.6,\ \beta = 1.0392]$

Number of points		Far-field boundary, δ^* units	ω_r	ω_i
First domain	Second domain			
37	21	15	0.496104813	$3.764828351 \times 10^{-3}$
37	31	30	.496104828	$3.764822175 \times 10^{-3}$
37	51	60	.496104848	$3.764817702 \times 10^{-3}$

Table V. Maximum Values of ω_i

Mach number	α	ω_i for —		
		$U_o = \tanh y$ (ref. 11)	$U_o = \tanh y$ (SPECLS)	$U_o = 0.5(1 + \tanh y)$ (SPECLS)
0	0.445	0.190	0.18954	0.094688
.1	.433	.187	.18736	
.2	.426	.181	.18112	
.3	.417	.171	.17105	
.4	.409	.158	.15760	
.5	.397	.141	.14101	
.6	.370	.122	.12180	
.7	.326	.101	.10012	
.8	.279	.078	.07760	
.9	.208	.055	.05450	
1.0	.000	.000	.00000	

Table VI. Sensitivity Analysis With Varying Boundary Layer Mean Flow Properties

$$\begin{bmatrix} M_\infty = 4.5,\ \mathrm{Re} = 10\,000,\ \alpha = 0.6,\ \beta = 1.0392 \\ \text{SPECLS discretization: SDSPD, 81 points} \end{bmatrix}$$

Case[a]	ω_r	ω_i	Mean flow	T_e, °R	σ	λ	Interpolation of mean flow onto SPECLS grid	Difference in ω_i; from case 1
1	0.497254134	$7.260461085 \times 10^{-3}$	Spectral (ref. 6)	300	0.72	$(-2/3)\mu$	Spectral	0%
2	.497308042	$7.219787293 \times 10^{-3}$	2nd order finite difference (ref. 7)	300	.72	$(-2/3)\mu$	Cubic spline	0.56%
3	.497308964	$7.218772535 \times 10^{-3}$	2nd order finite difference (ref. 7)	300	.72	$(-2/3)\mu$	Linear	0.57%
4	.49725909	$7.269563811 \times 10^{-3}$	Spectral (ref. 6)	300	.72	$(4/30)\mu$	Spectral	0.13%
5	.496759786	$5.883195138 \times 10^{-3}$	Spectral (ref. 6)	300	.7	$(-2/3)\mu$	Spectral	20%
6	.496601687	$5.149929437 \times 10^{-3}$	Spectral (ref. 6)	520	.72	$(-2/3)\mu$	Spectral	30%
7	.496093364	$3.761833505 \times 10^{-3}$	Spectral (ref. 6)	520	.7	$(-2/3)\mu$	Spectral	48%

[a]Underlined entries denote property changed relative to case 1.

Table VII. Effect of Stretching Parameter C_2 in SPECLS

$[M_\infty = 1.0,\ \mathrm{Re} = 10\,000,\ \beta_T = 0.2,\ \alpha = 5,\ \beta = 0]$

(a) Single-domain: 99 points on [–100, 100]

Stretching parameter	ω_r	ω_i
1.1	1.47179	0.272236
1.2	1.49883	.159461
1.3	1.49806	.158226
1.4	1.57814	.266635

(b) Multi-domain: 17 points on [–100, –1], 65 points on [–1, 1], 17 points on [1, 100]

Stretching parameter	ω_r	ω_i
1.6	1.497268	0.167511
2.0	1.496913	.159498
2.2	1.497146	.158781
4.0	1.496359	.156986

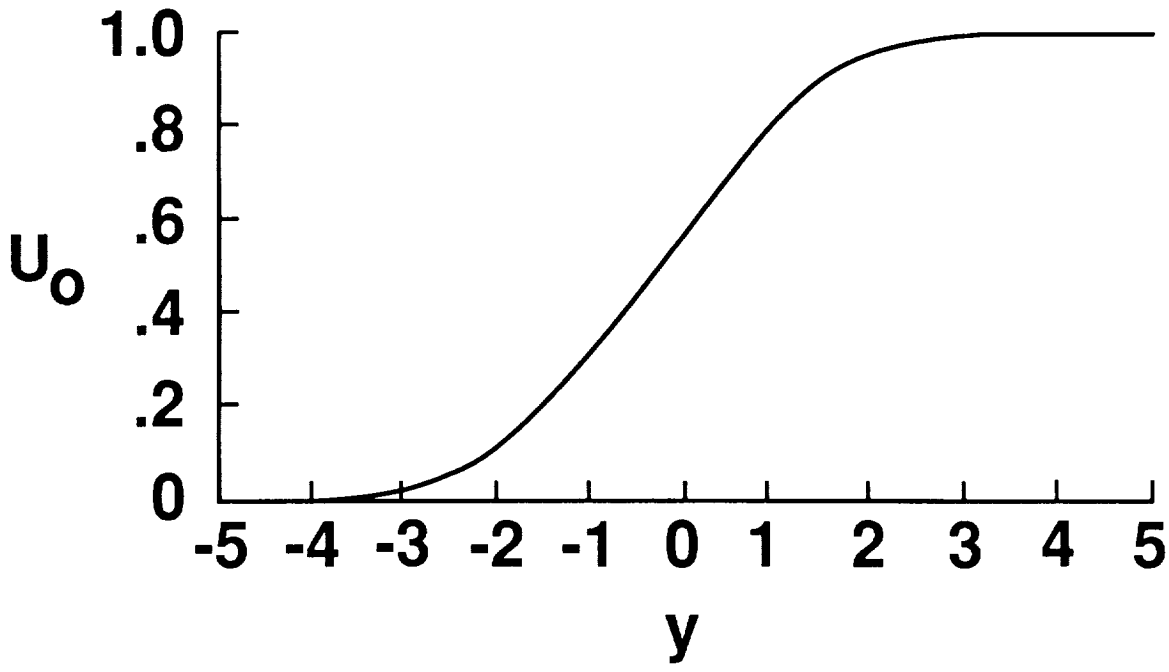

Figure 1. Streamwise-velocity profile of mean flow for free shear layer.

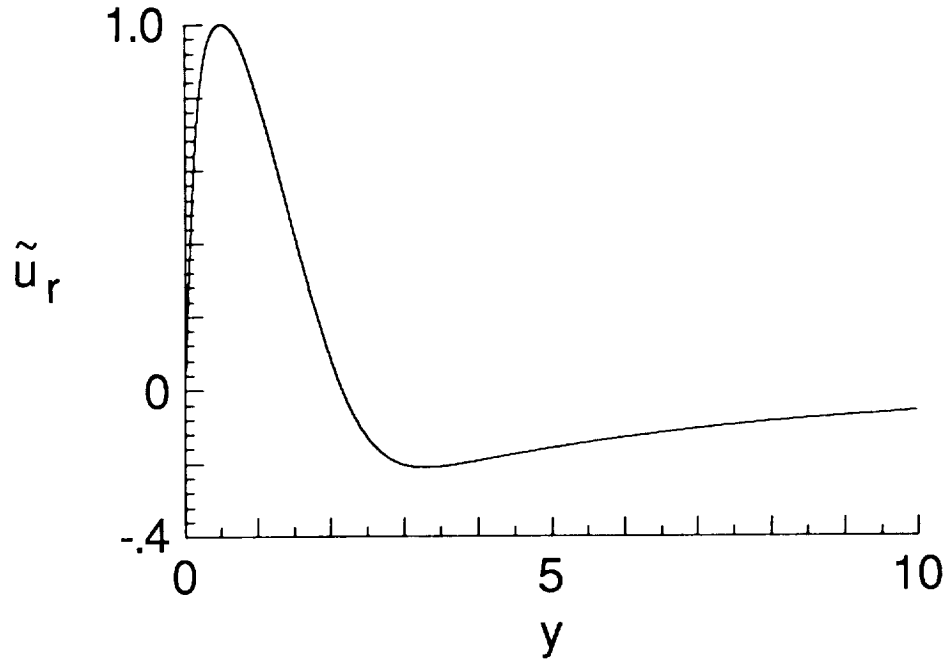

(a) Calculation by SPECLS.

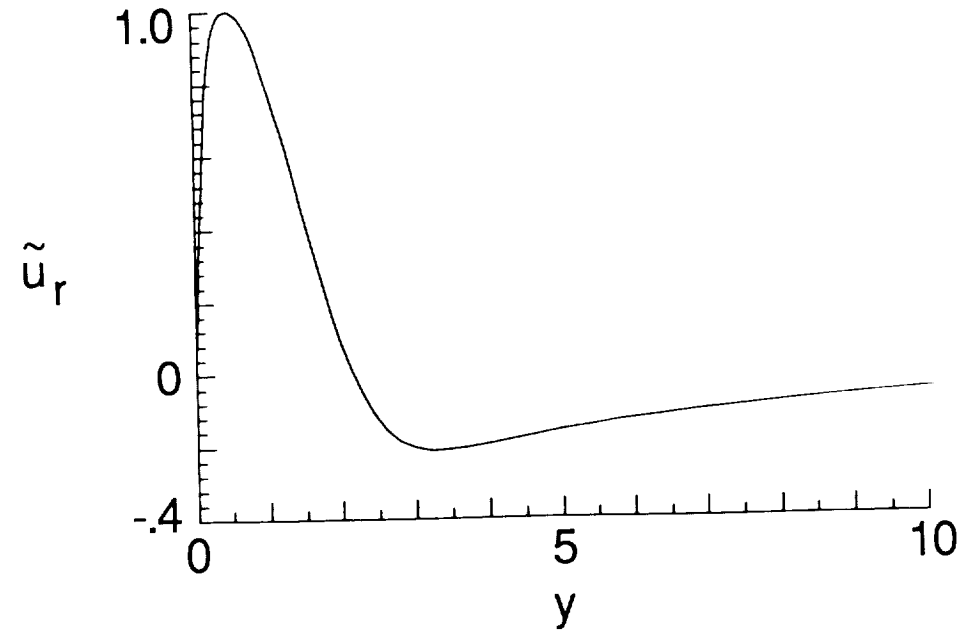

(b) Calculation by COSAL.

Figure 2. Streamwise-velocity fluctuation $\tilde{u}$ for $\alpha = 0.2$, $\beta = 0$, $M_\infty = 0.00001$, Re $= 2200$, and $T_e = 520°$R.

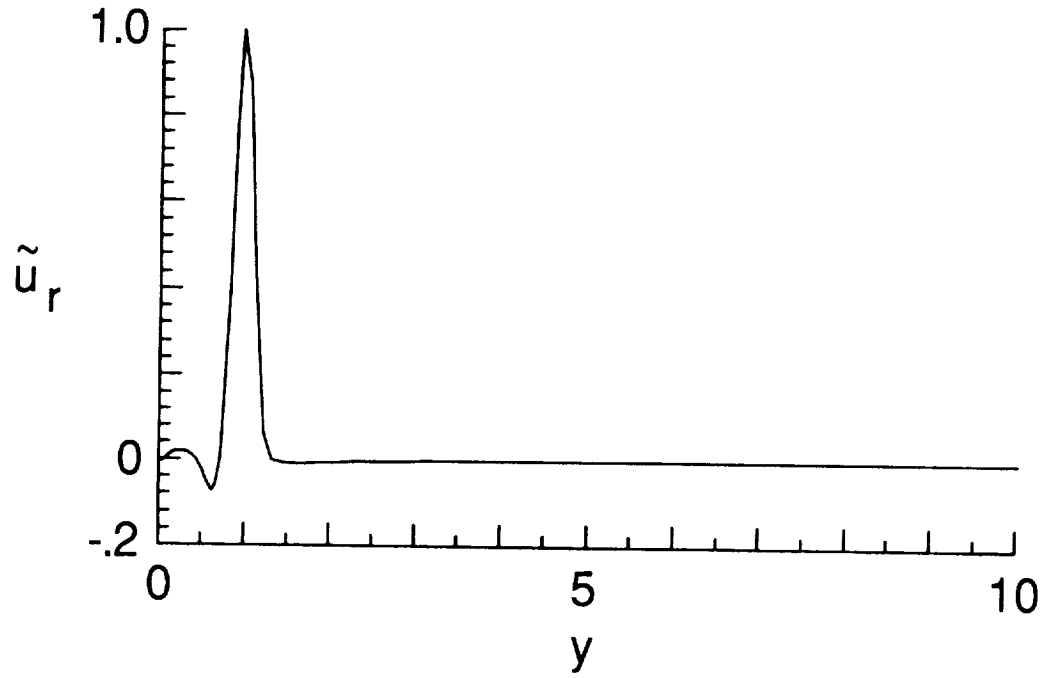

(a) Calculation by SPECLS.

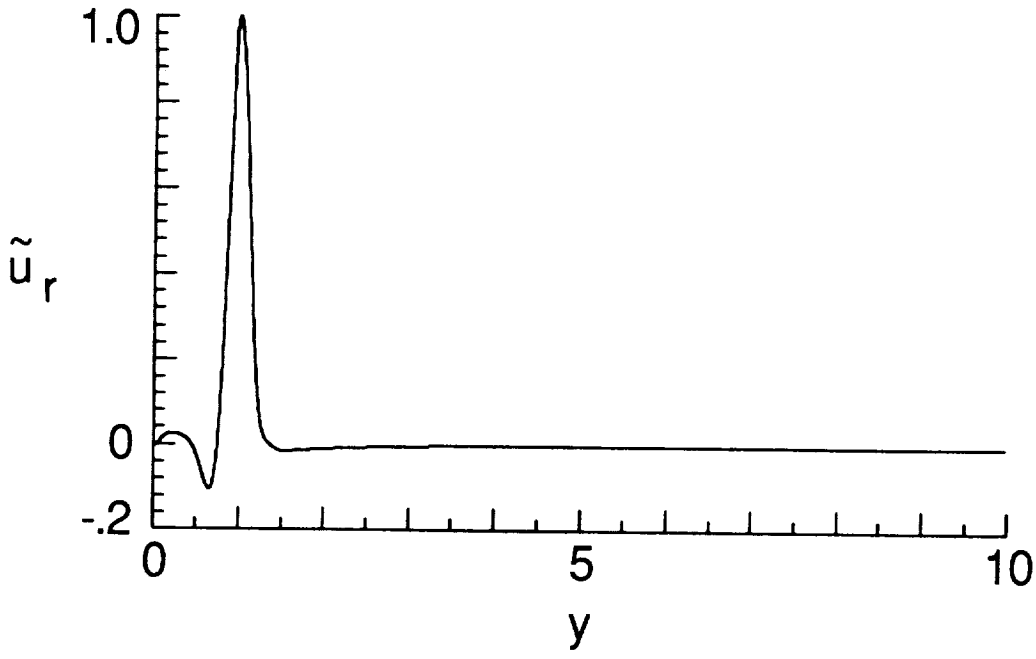

(b) Calculation by COSAL.

Figure 3. Streamwise-velocity fluctuation $\tilde{u}$ for $\alpha = 0.6$, $\beta = 1.0392$, $M_\infty = 4.5$, Re $= 10\,000$, and $T_e = 520°$R.

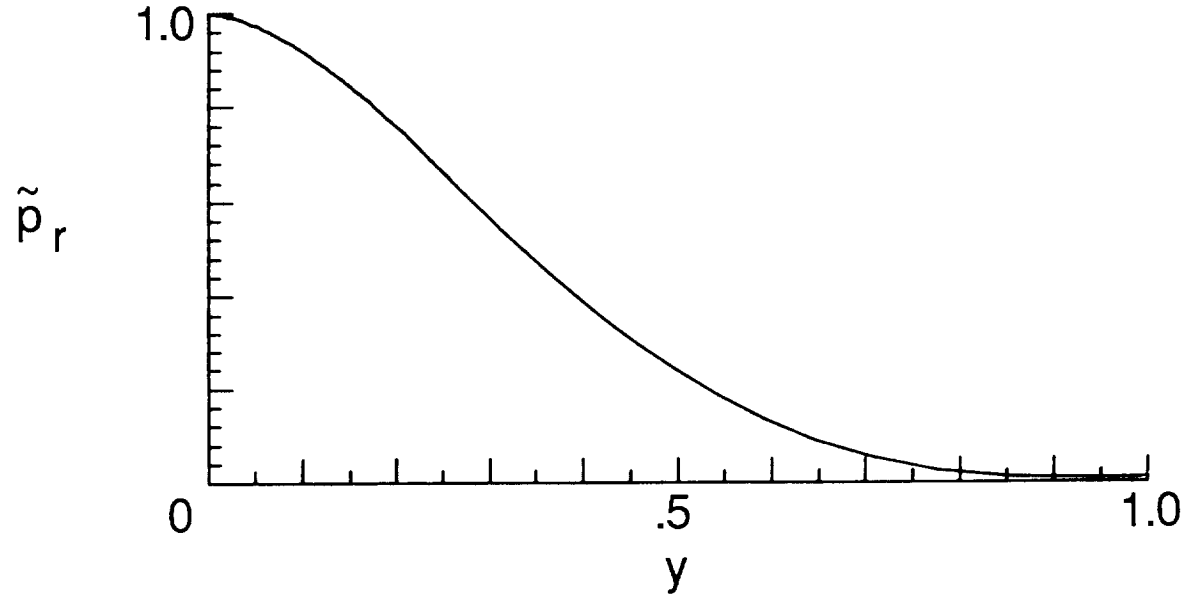

(a) Calculation by SPECLS (Re = 100 000).

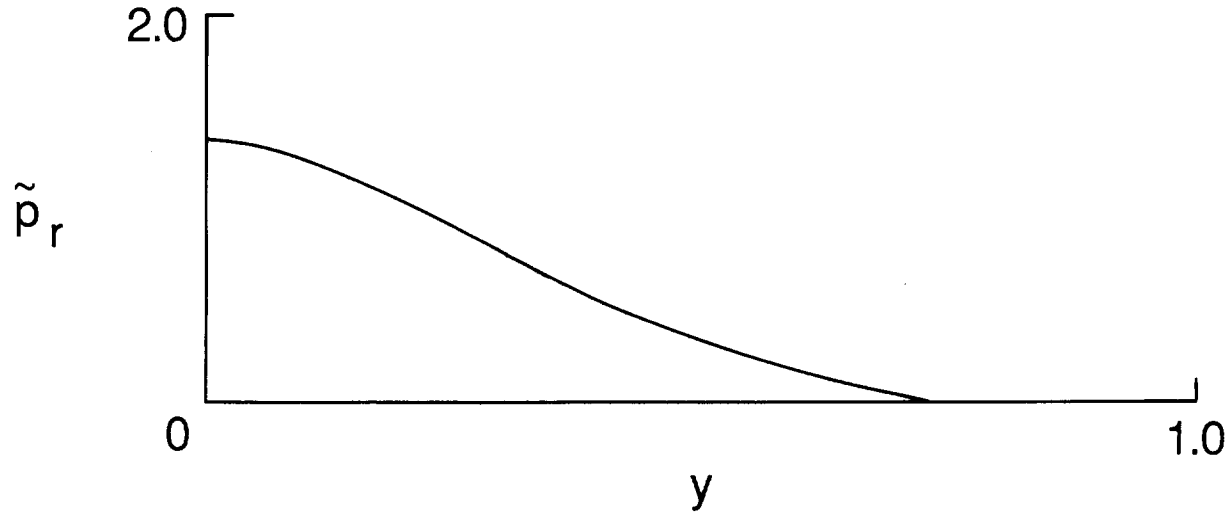

(b) Solution from reference 2 (inviscid).

Figure 4. Pressure fluctuation $\tilde{p}$ for the first mode of neutral subsonic solution at $\alpha = 1.844$, $\beta = 0$, $M_\infty = 10$, and $T_e = 90°\text{R}$.

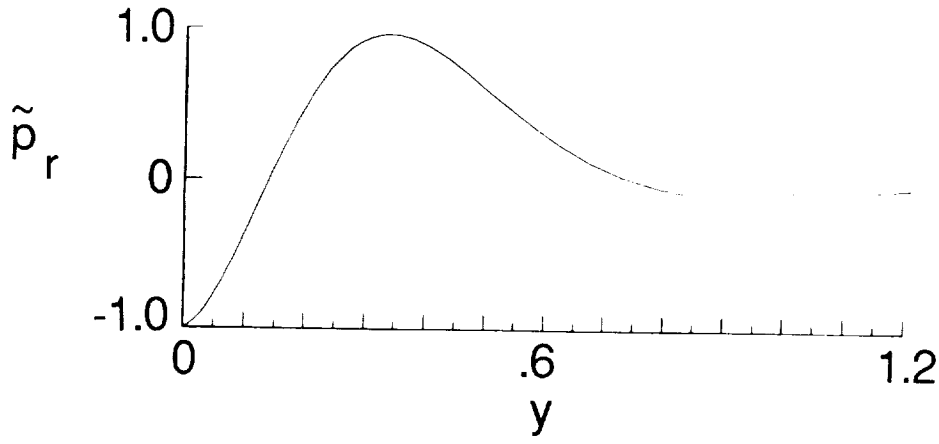

(a) Calculation by SPECLS (Re = 100 000).

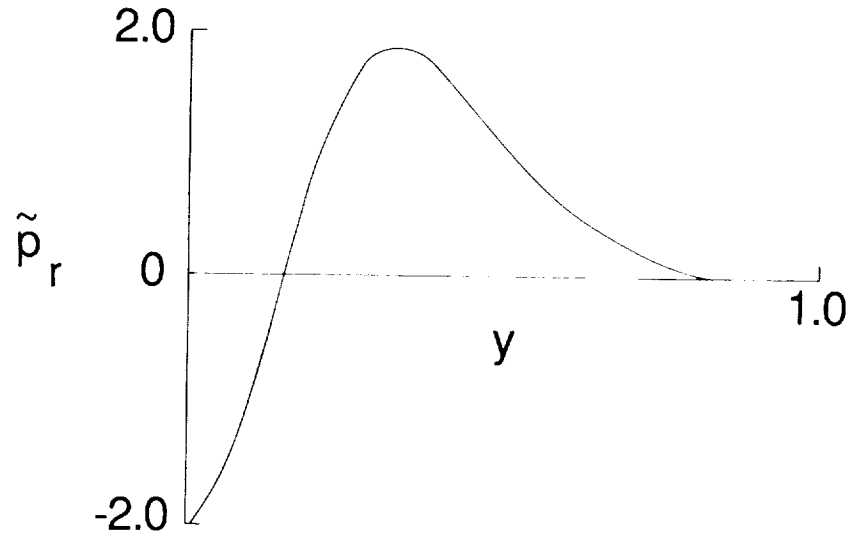

(b) Solution from ref. 2 (inviscid).

Figure 5. Pressure fluctuation $\tilde{p}$ for the second mode of neutral subsonic solution at $\alpha = 4.9877$, $\beta = 0$, $M_\infty = 10$, and $T_e = 90°\mathrm{R}$.

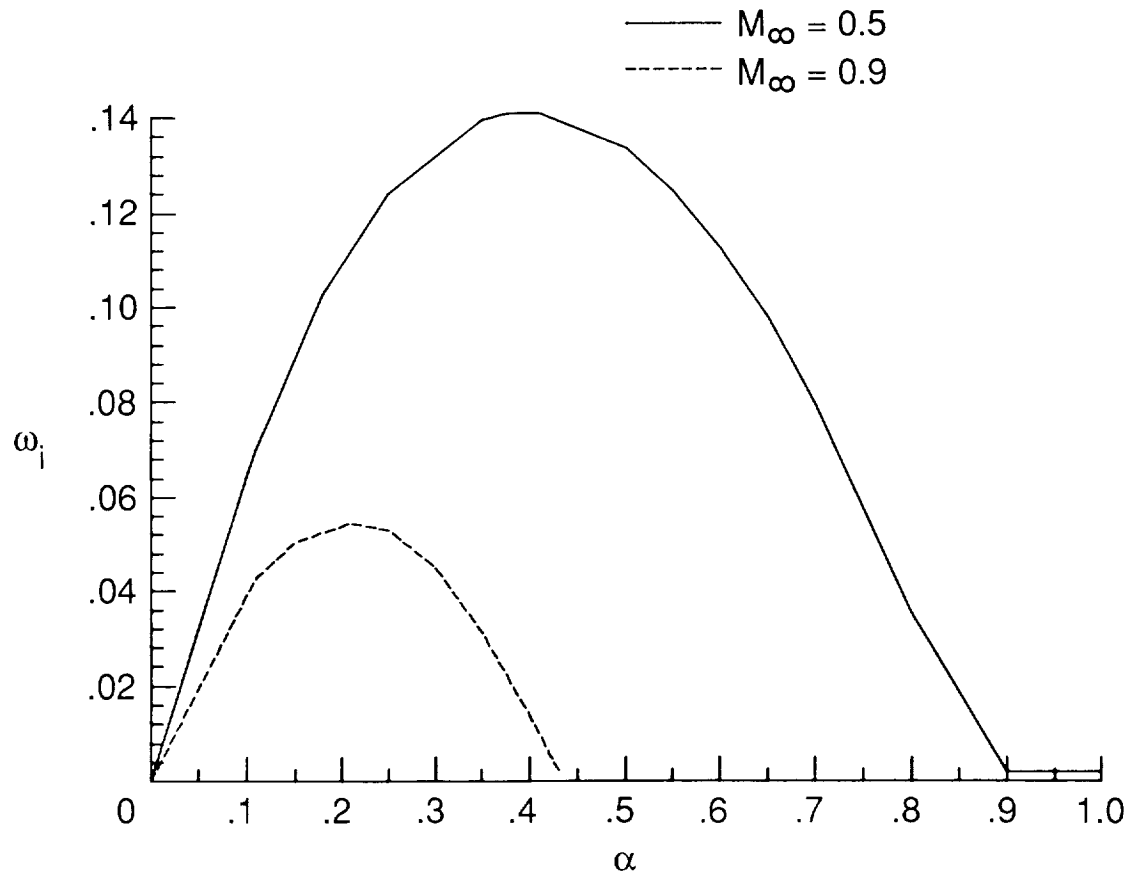

Figure 6. Effect of Mach number on growth rate versus wave number α for the hyperbolic tangent mean flow profile. Re = 10 000.

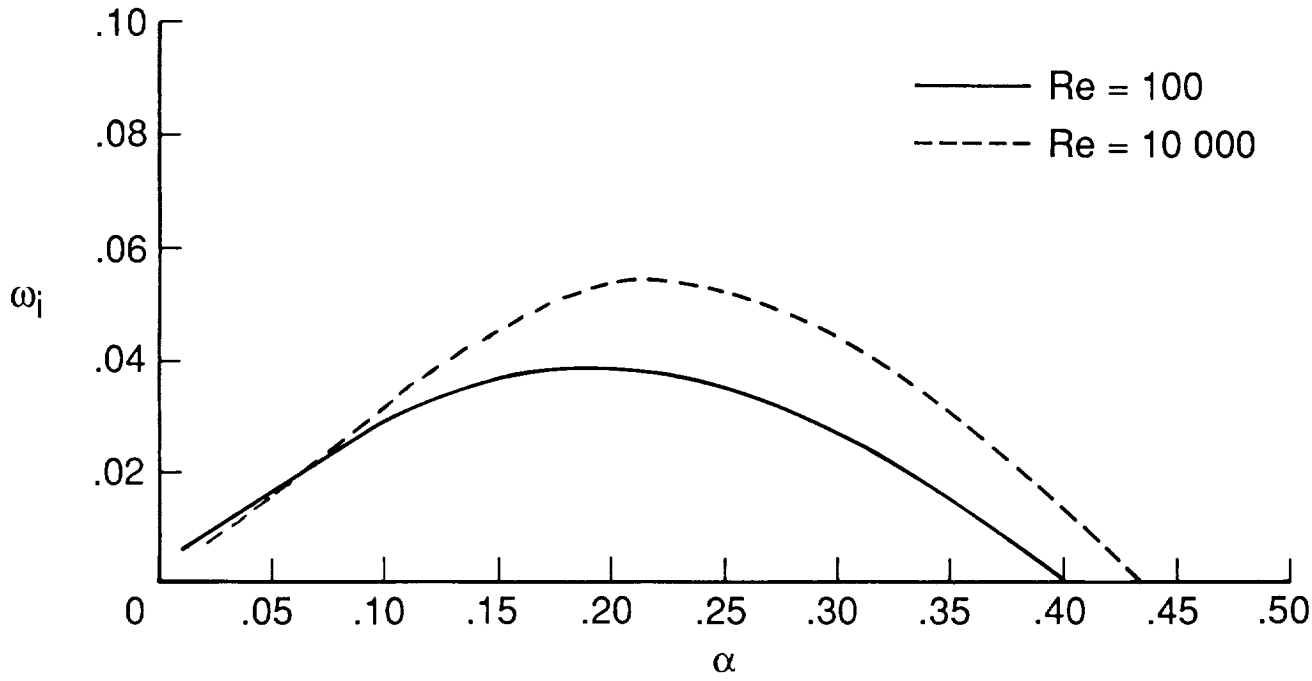

Figure 7. Effect of Reynolds number on growth rate versus wave number α for the hyperbolic tangent mean flow profile. $M_\infty = 0.9$.

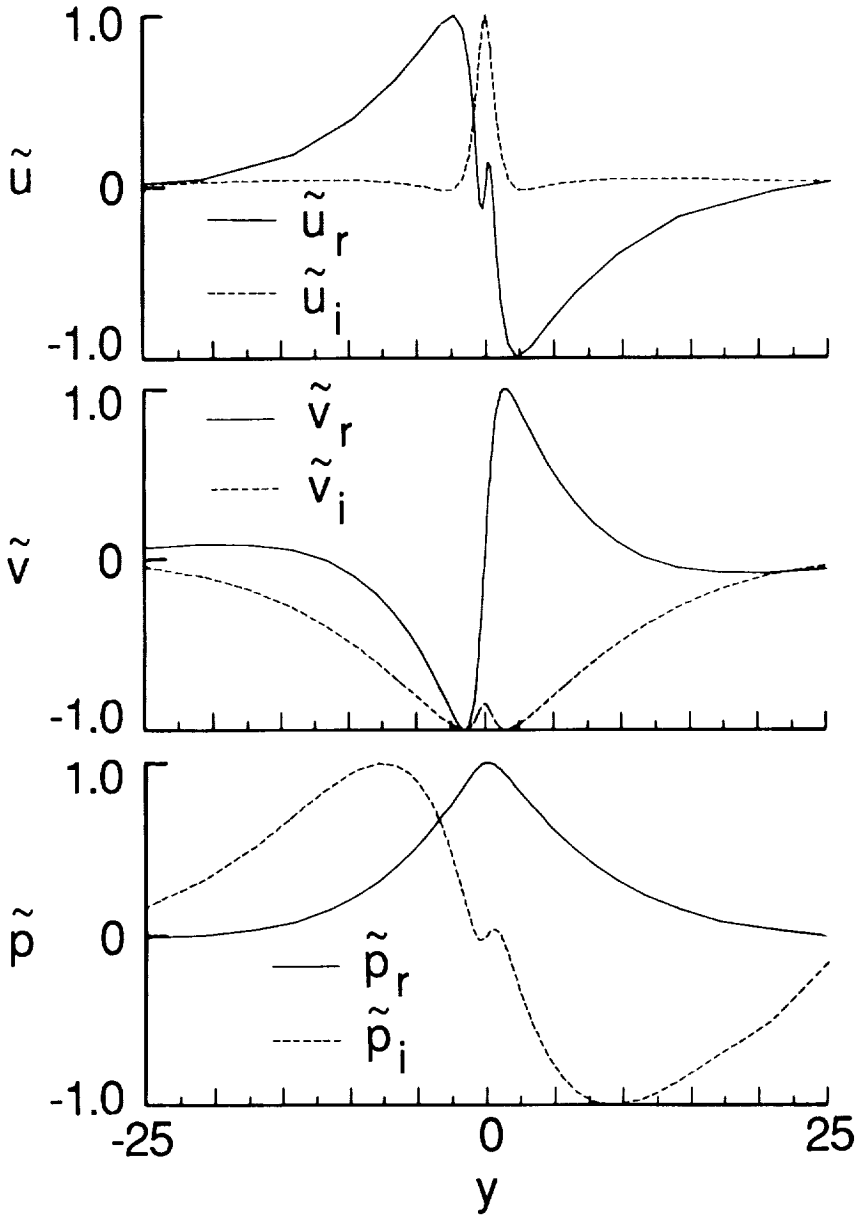

Figure 8. Complex disturbances versus y for the hyperbolic tangent mean flow profile at the maximum growth rate. $M_\infty = 0.9$; Re = 10 000.

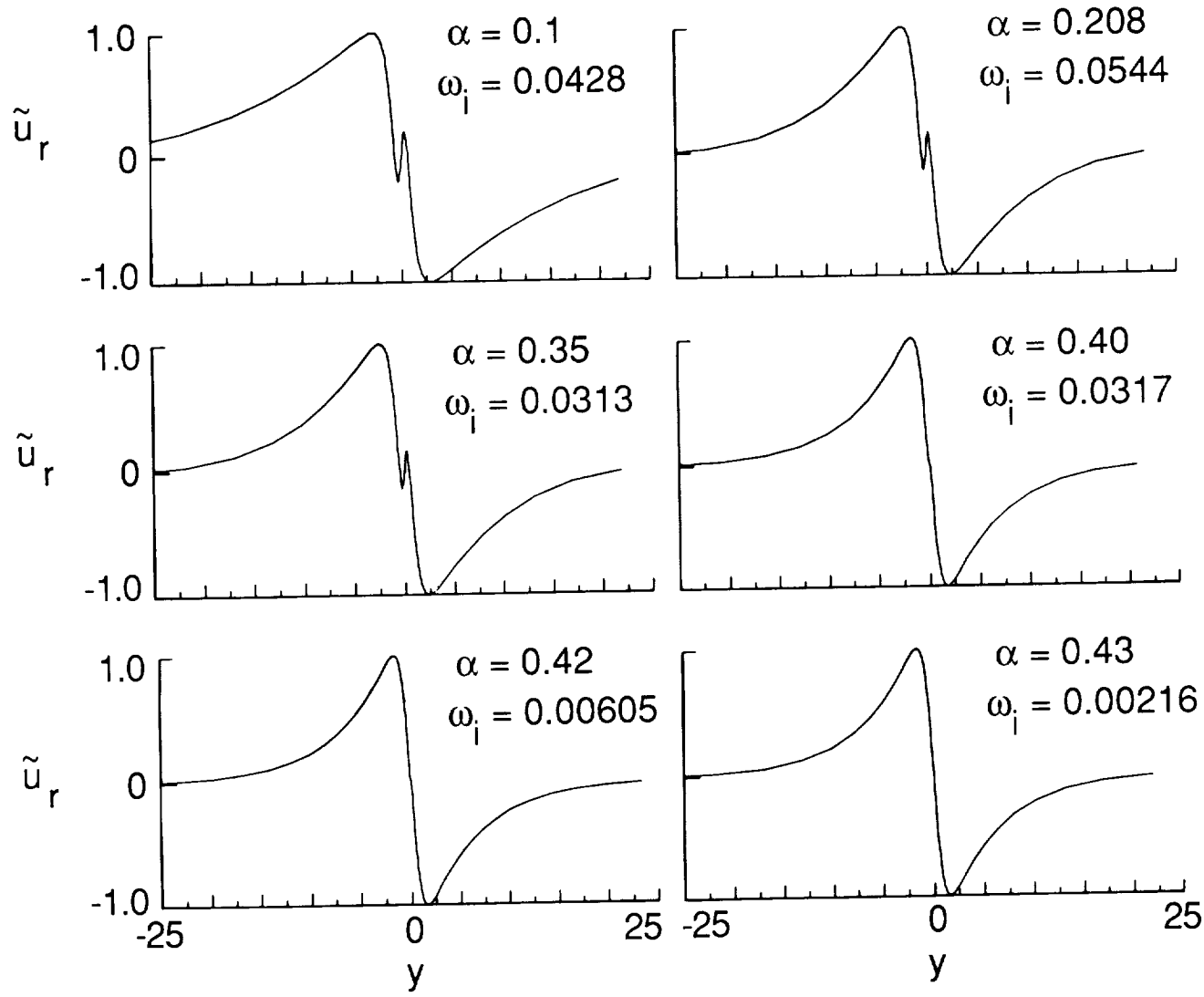

Figure 9. Streamwise-velocity fluctuation $\tilde{u}$ for increasing α for the hyperbolic tangent mean flow profile. $M_\infty = 0.9$; Re = 10 000.

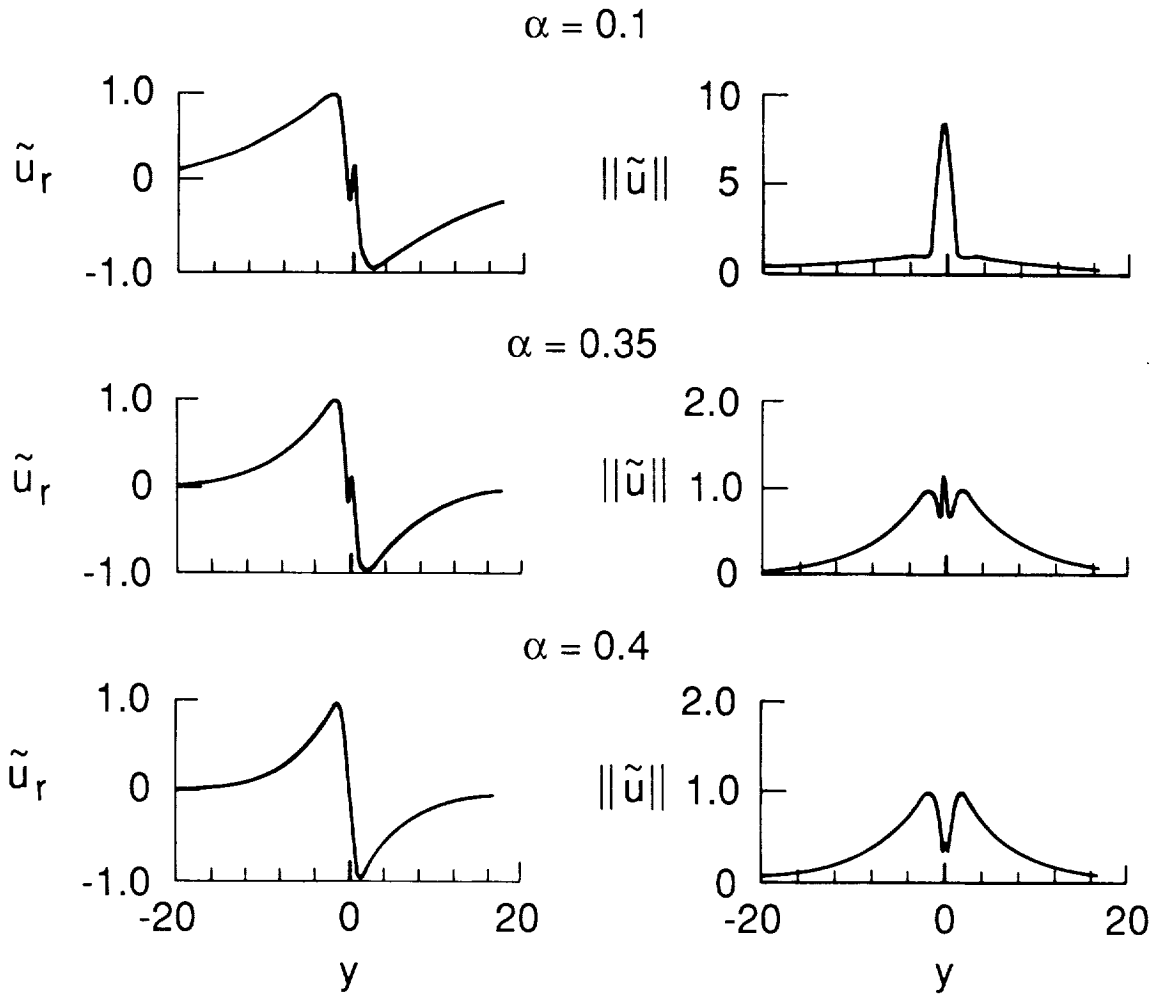

Figure 10. Plots of $\tilde{u}_r$ and $\|\tilde{u}\|$ for increasing α. $M_\infty = 0.9$; Re = 10 000.

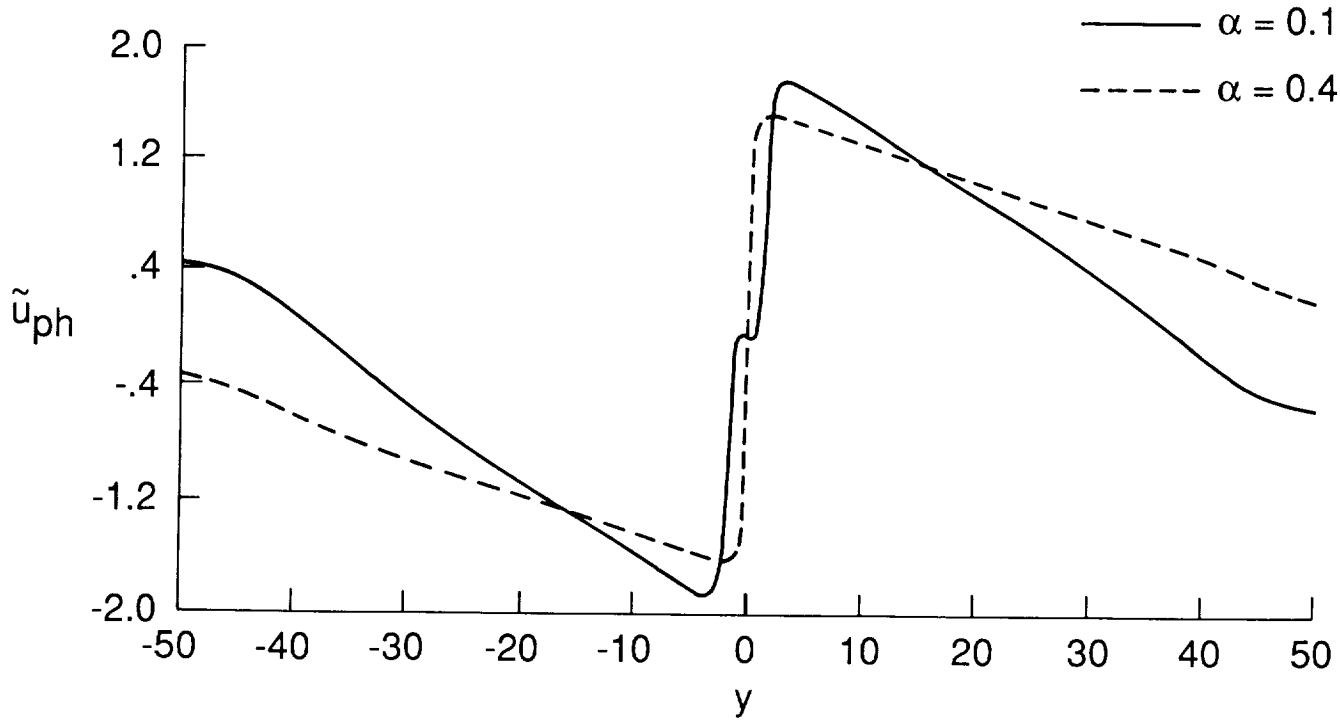

Figure 11. Plots of phase of $\tilde{u}$ corresponding to the $\alpha = 0.1$ and $\alpha = 0.4$ cases given in figure 9.

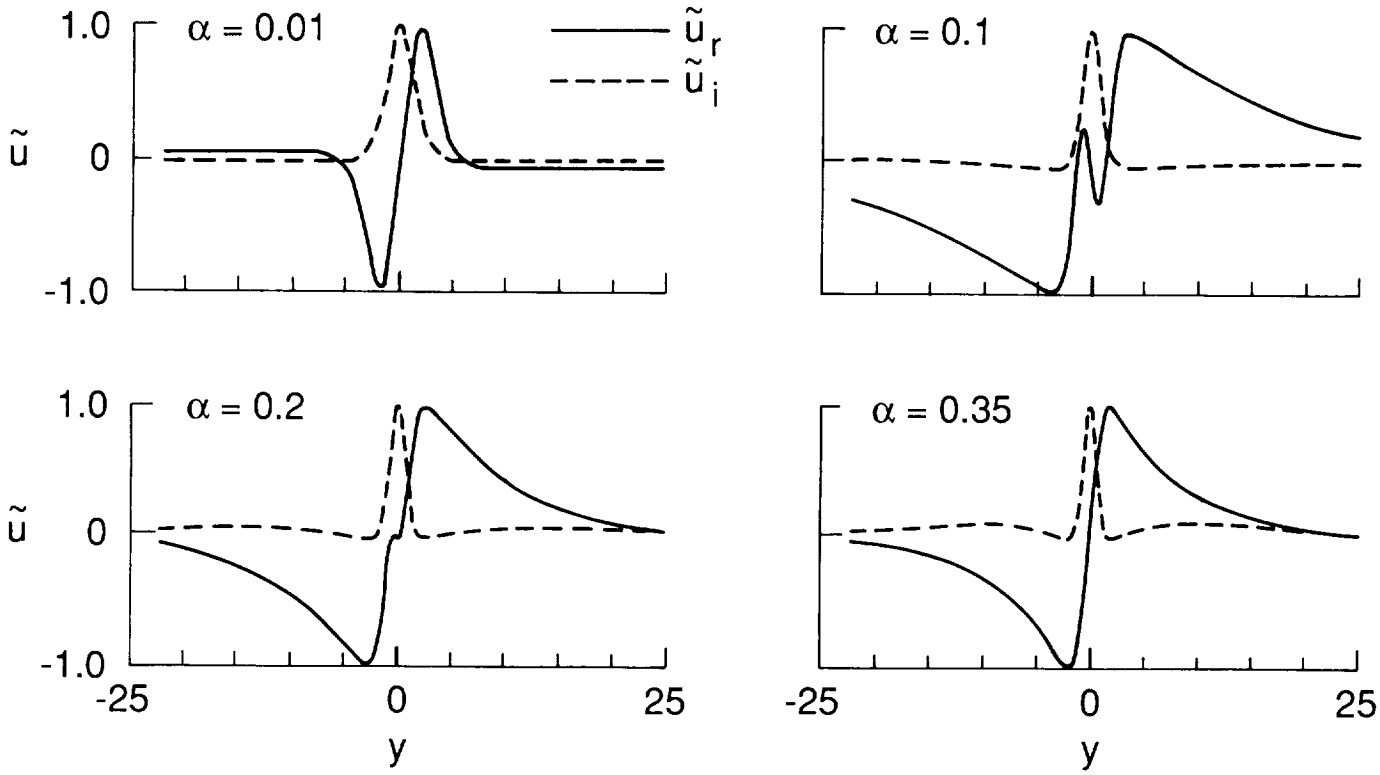

Figure 12. Streamwise-velocity disturbances $\tilde{u}$ for increasing α for the hyperbolic tangent mean flow profile. $M_\infty = 0.9$; Re = 100; $\beta = 0$.

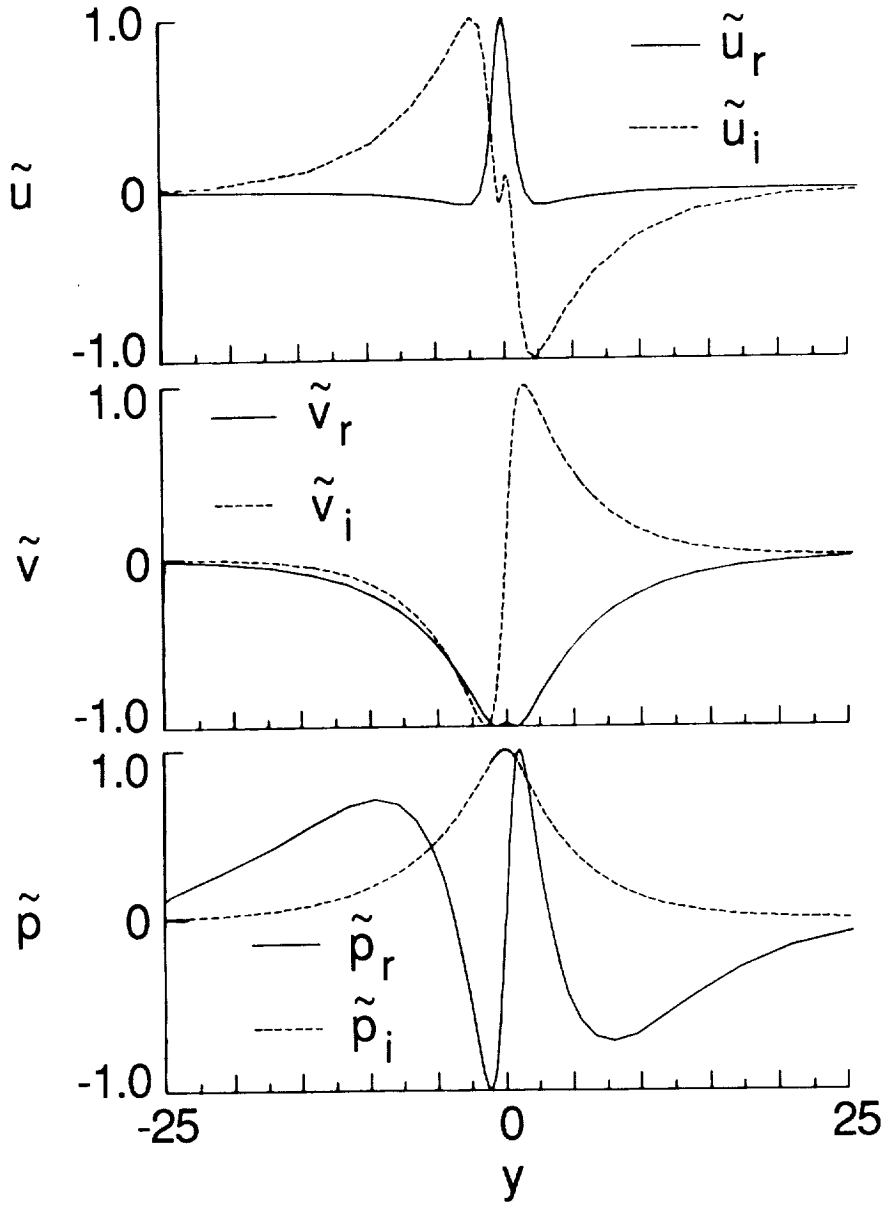

Figure 13. Complex disturbances versus y for $U_o = 0.5(1 + \tanh y)$. $M_\infty = 0.9$; Re = 10 000; $\alpha = 0.208$; $\beta = 0$.

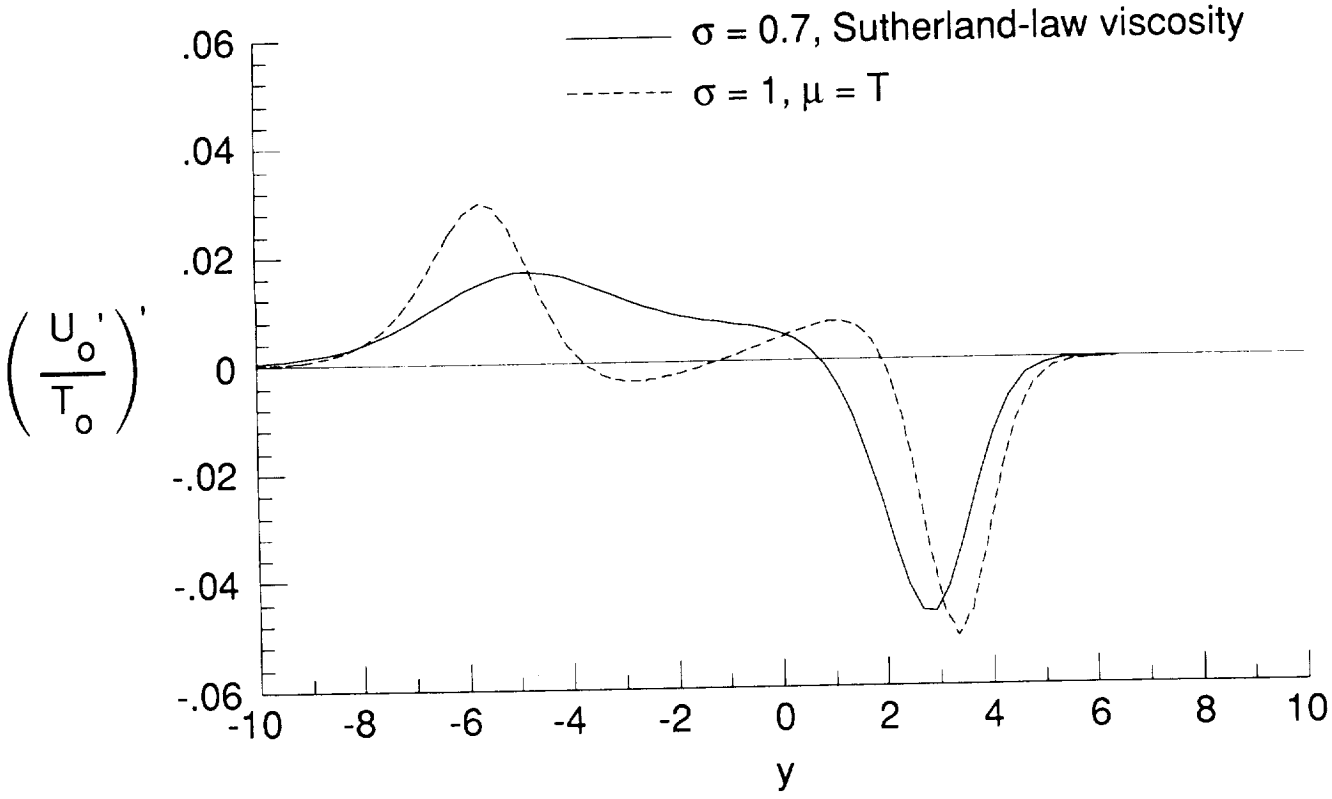

Figure 14. Plot of the function $(U_o'/T_o)'$ versus y for two shear layer mean flows. $M_\infty = 5$; $\beta_T = 0.6$.

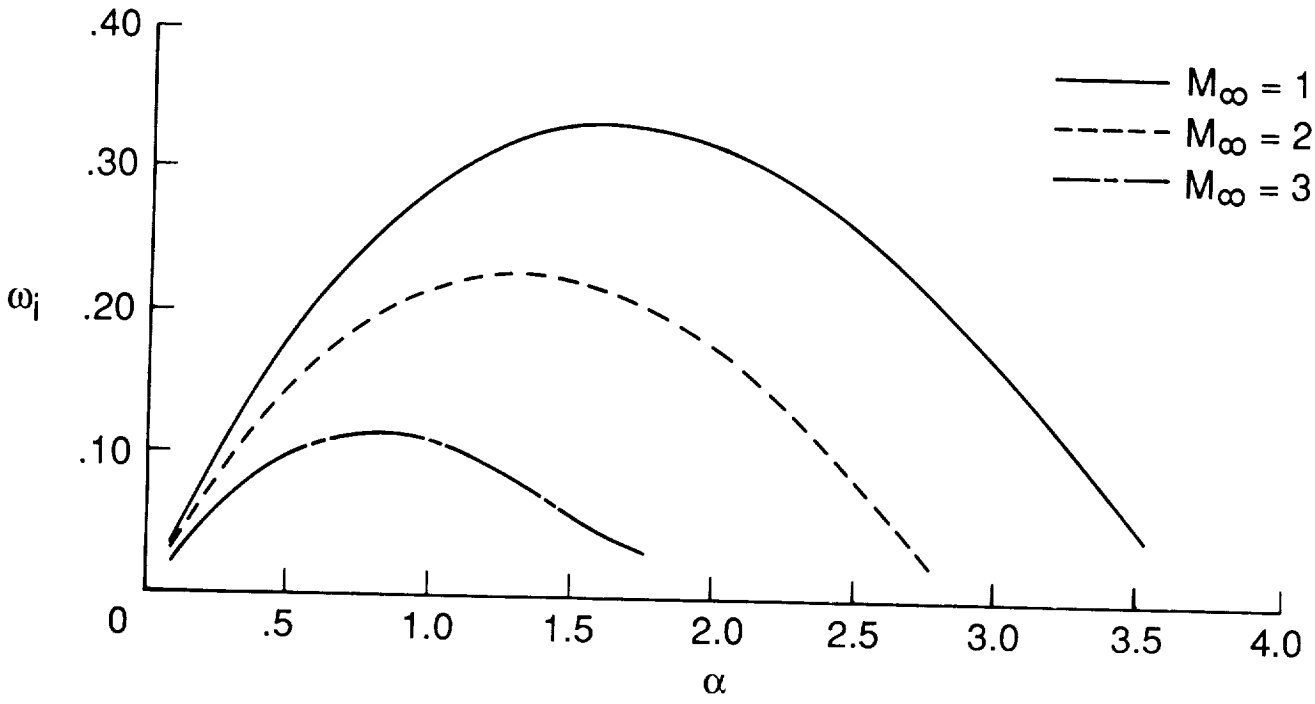

Figure 15. Growth rate versus wave number α for a range of Mach numbers. $\theta = 60°$.

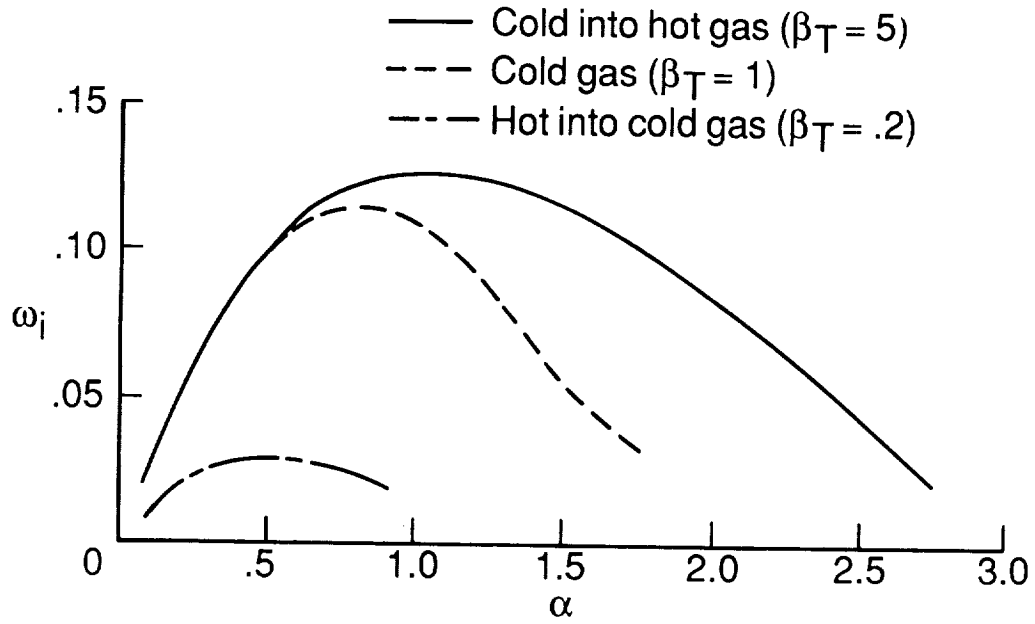

Figure 16. Growth rate versus wave number α for various temperatures. $M_\infty = 3$; $\theta = 60°$.

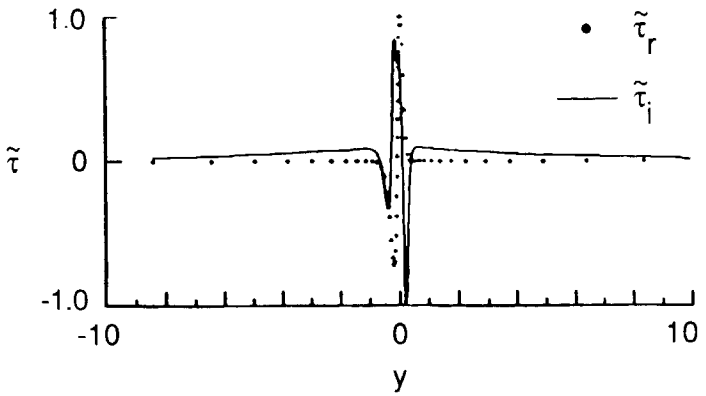

(a) Cold injection (500°R) into a hot gas (2500°R), $\beta_T = 5$.

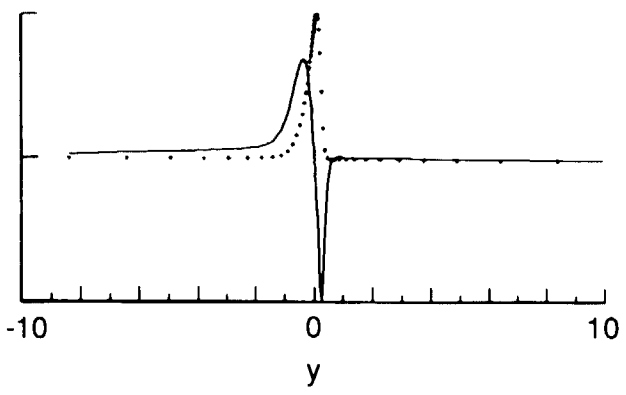

(c) Hot injection into a hot gas (2500°R), $\beta_T = 1$.

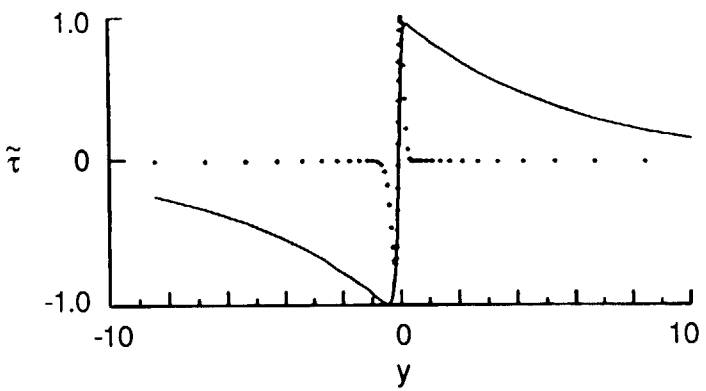

(b) Cold injection into a cold gas (520°R), $\beta_T = 1$.

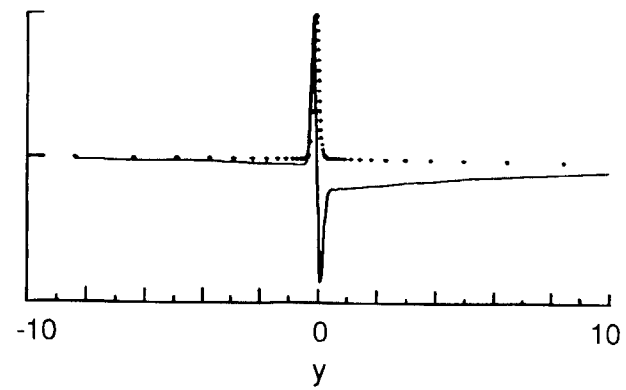

(d) Hot injection (2500°R) into a cold gas (500°R), $\beta_T = 0.2$.

Figure 17. Effect of temperature on temperature disturbance $\tilde{\tau}$. $M_\infty = 2; \theta = 60°$.

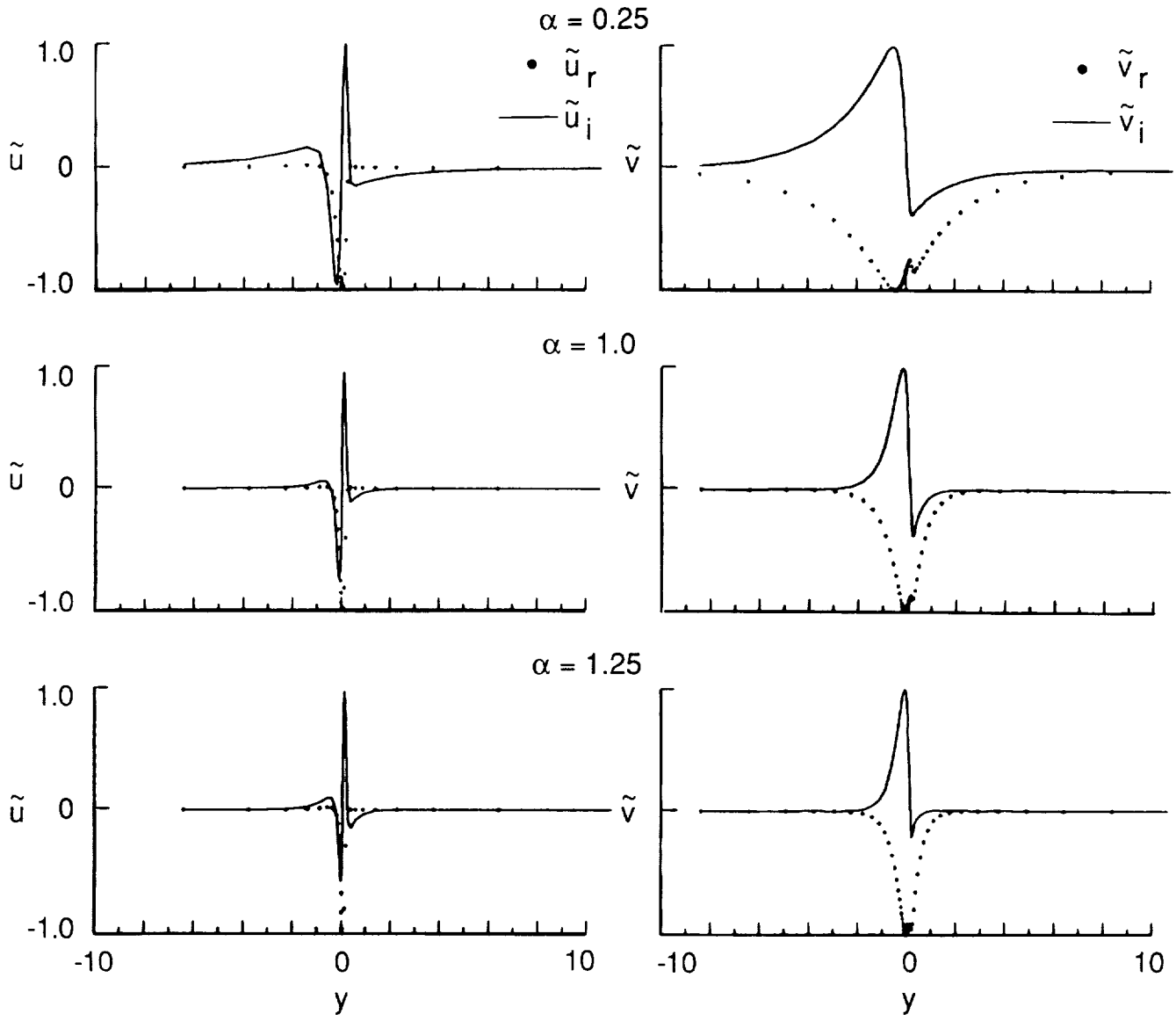

Figure 18. Effect of increasing α on $\tilde{u}$ and $\tilde{v}$ disturbances. $\theta = 60°$; $M_\infty = 3$.

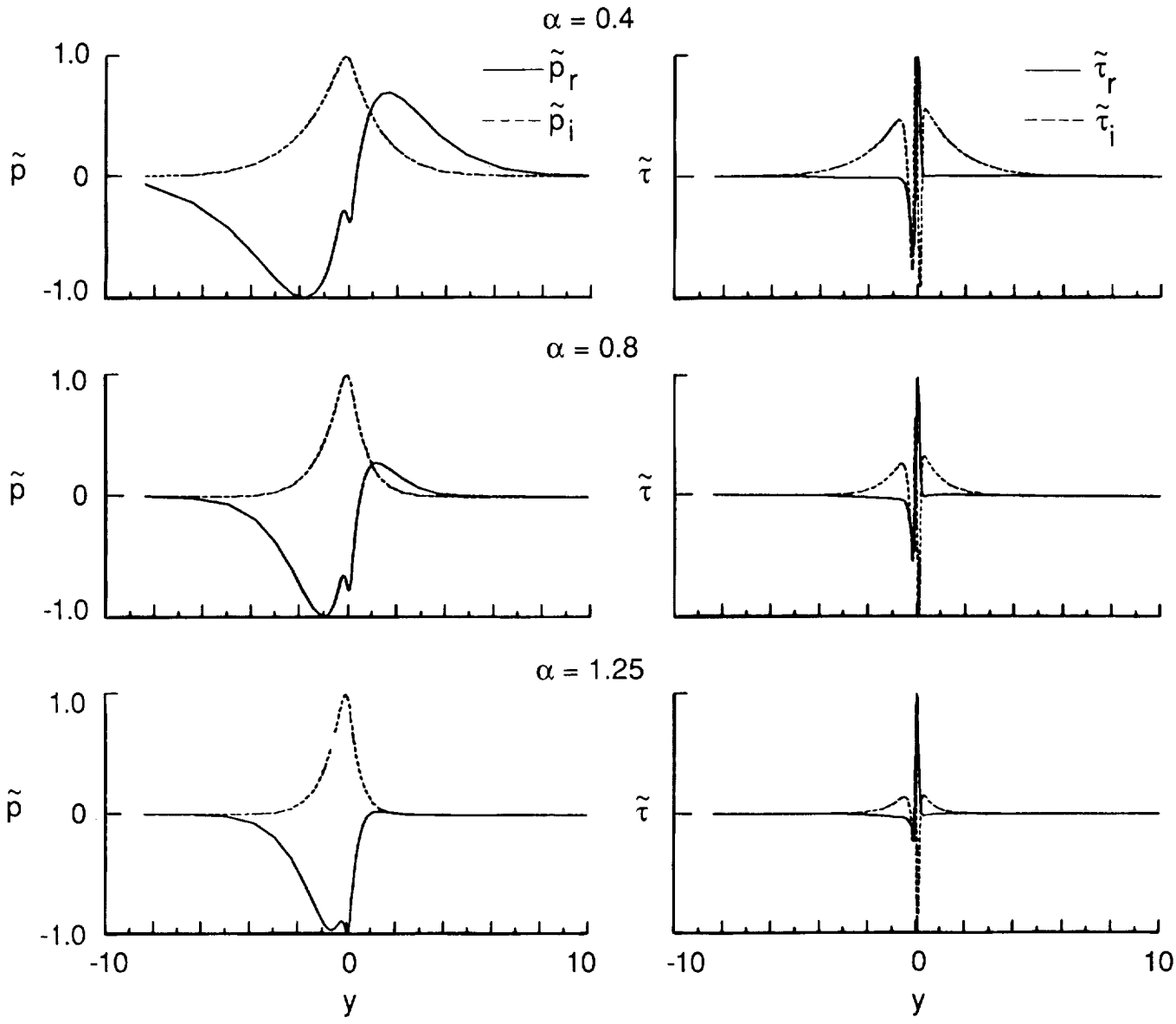

Figure 19. Effect of increasing α on $\tilde{p}$ and $\tilde{\tau}$ disturbances. $\theta = 60°$; $M_\infty = 3$.

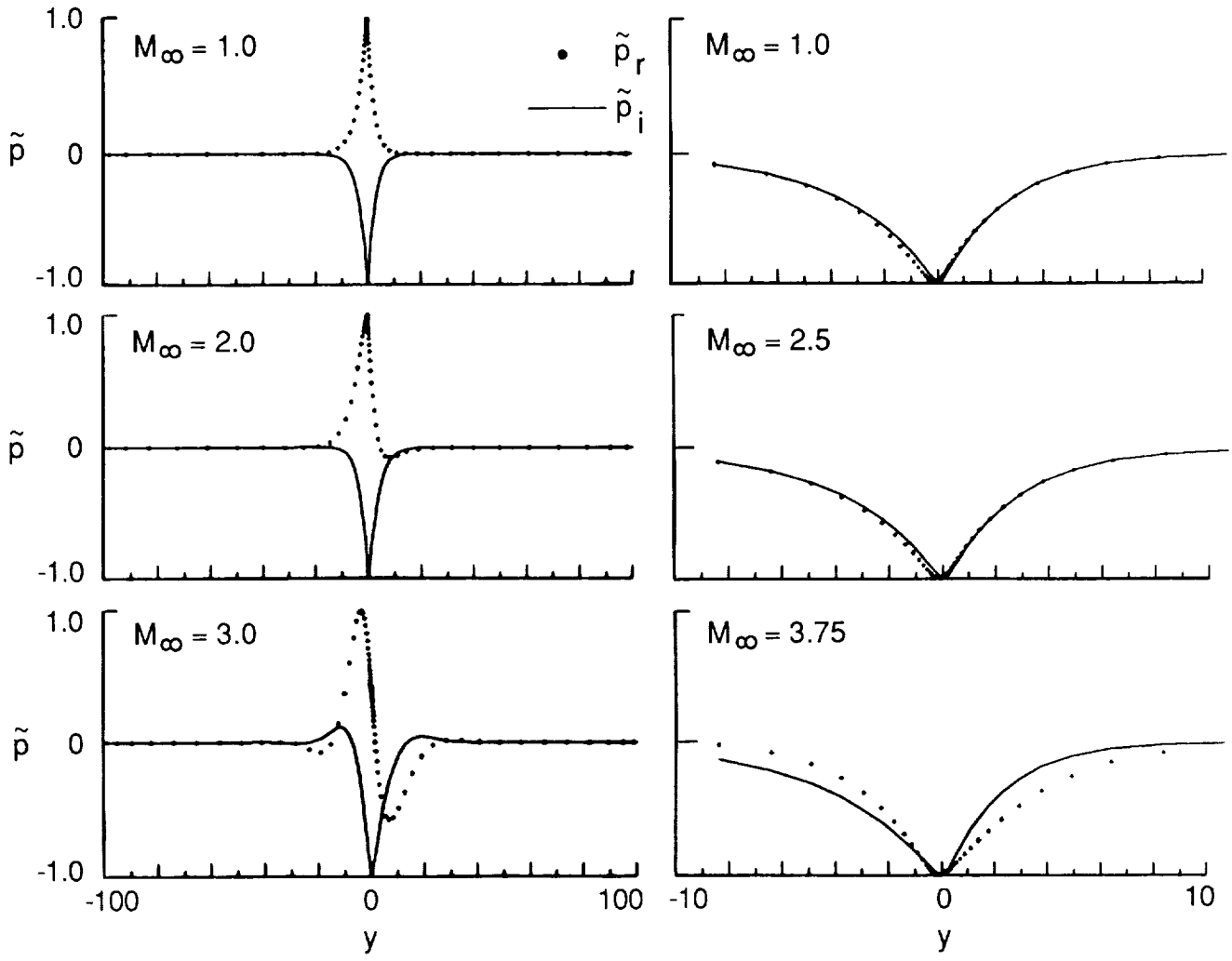

(a) $\beta_T = 0.2$.

(b) $\beta_T = 5$.

Figure 20. Pressure disturbance $\tilde{p}$ for increasing Mach number.

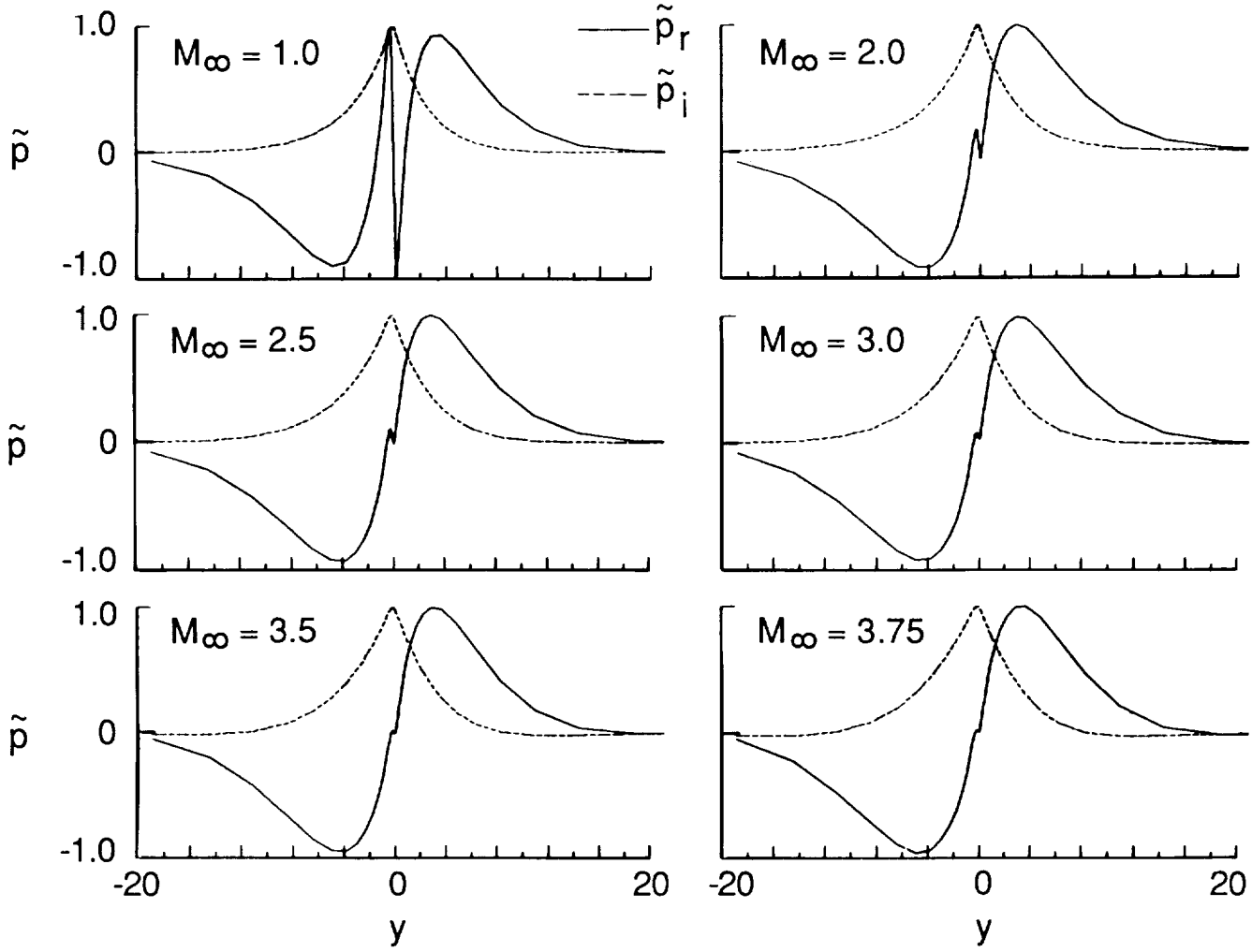

(c) $\beta_T = 1$.

Figure 20. Concluded.

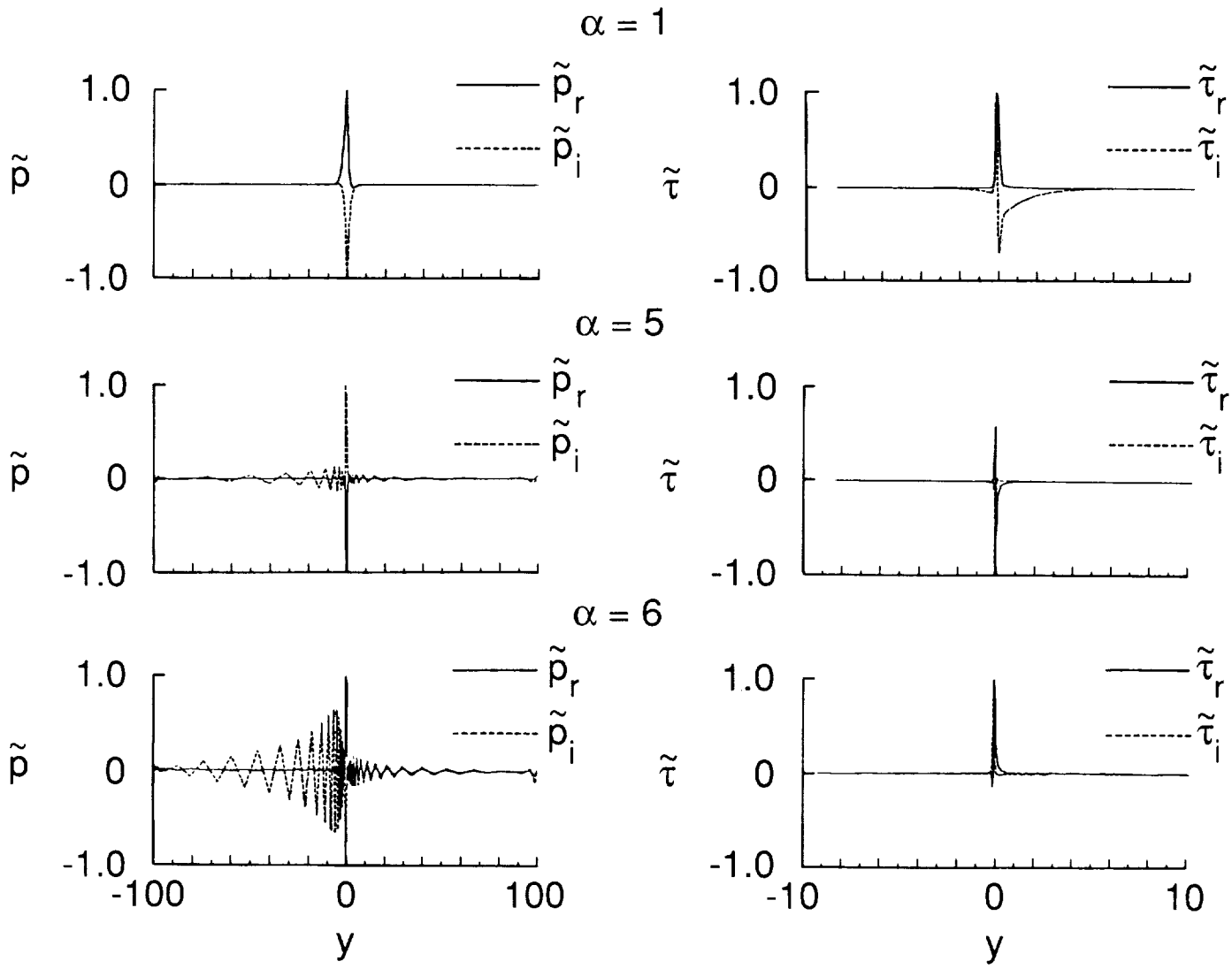

Figure 21. Effect of increasing α on $\tilde{p}$ and $\tilde{\tau}$ for two-dimensional disturbance ($\beta = 0$). $M_\infty = 1$; $\beta_T = 0.2$.

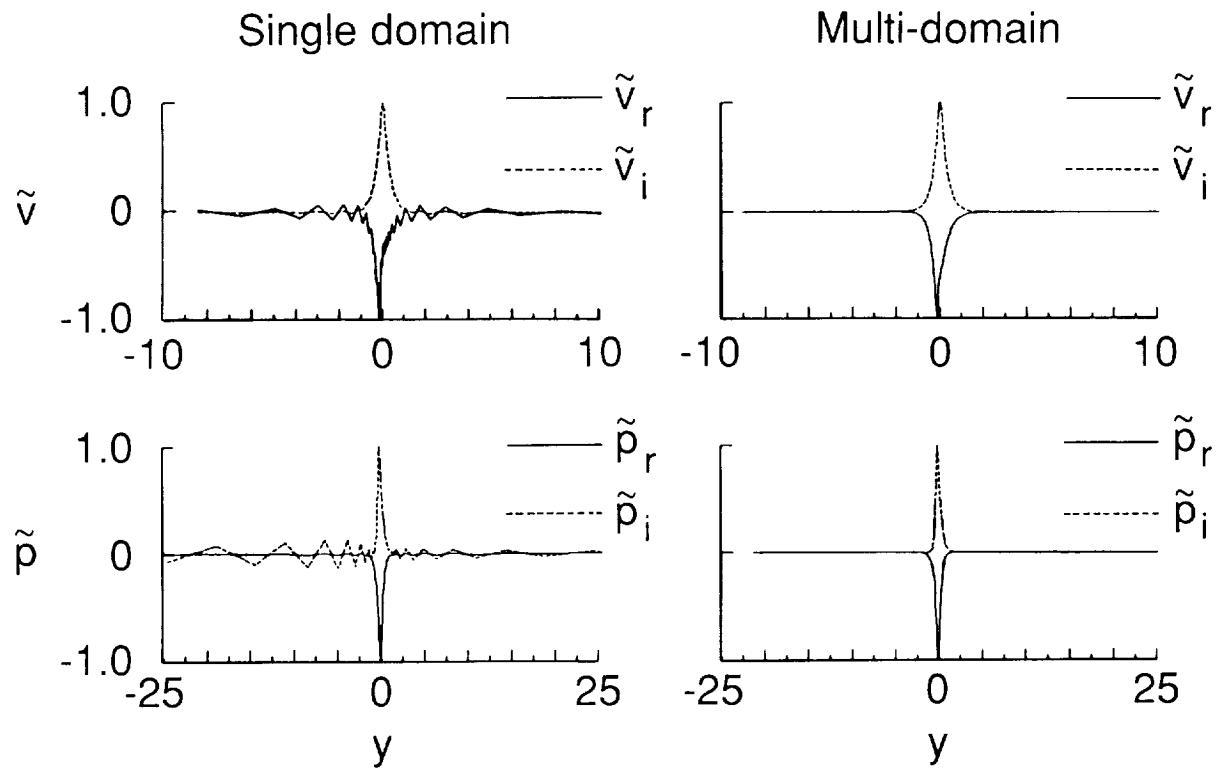

Figure 22. Disturbances $\tilde{v}$ and $\tilde{p}$ obtained with MDSPD and SDSPD in SPECLS for the case described in figure 21. $\alpha = 5$.

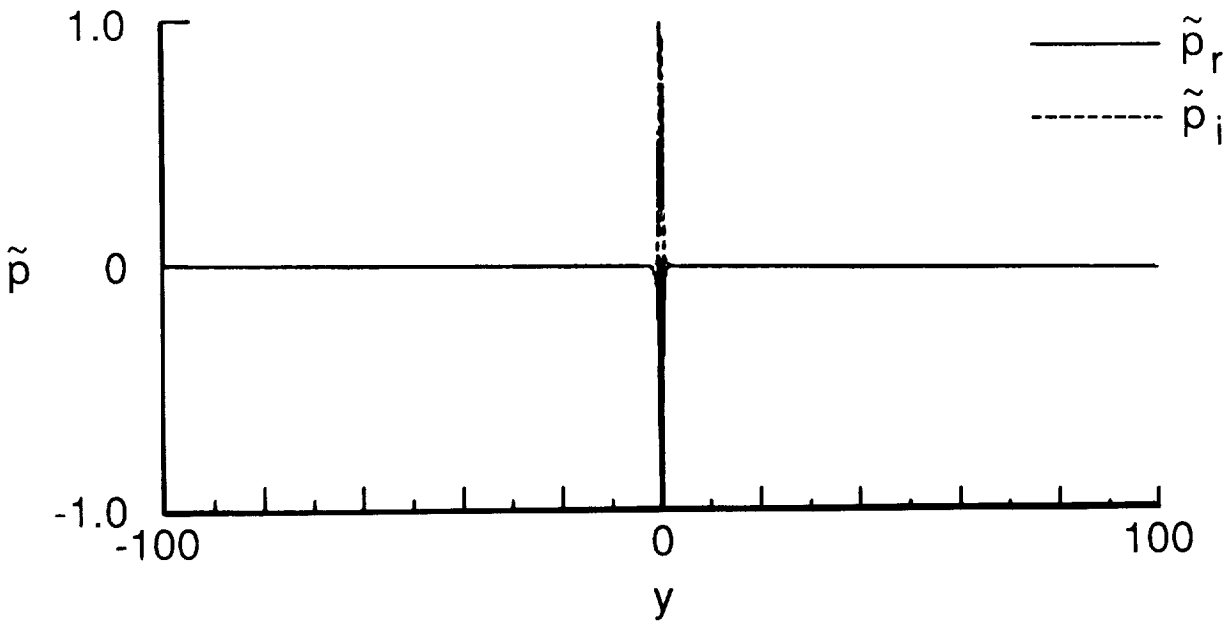

Figure 23. Pressure disturbance $\tilde{p}$ obtained with MDSPD in SPECLS displayed on entire computational domain for case of figure 21 for $\alpha = 5$. Discretization: center domain on [-.5,5], 41 points; left domain on [-100,-.5], 21 points; right domain on [.5,100], 35 points.

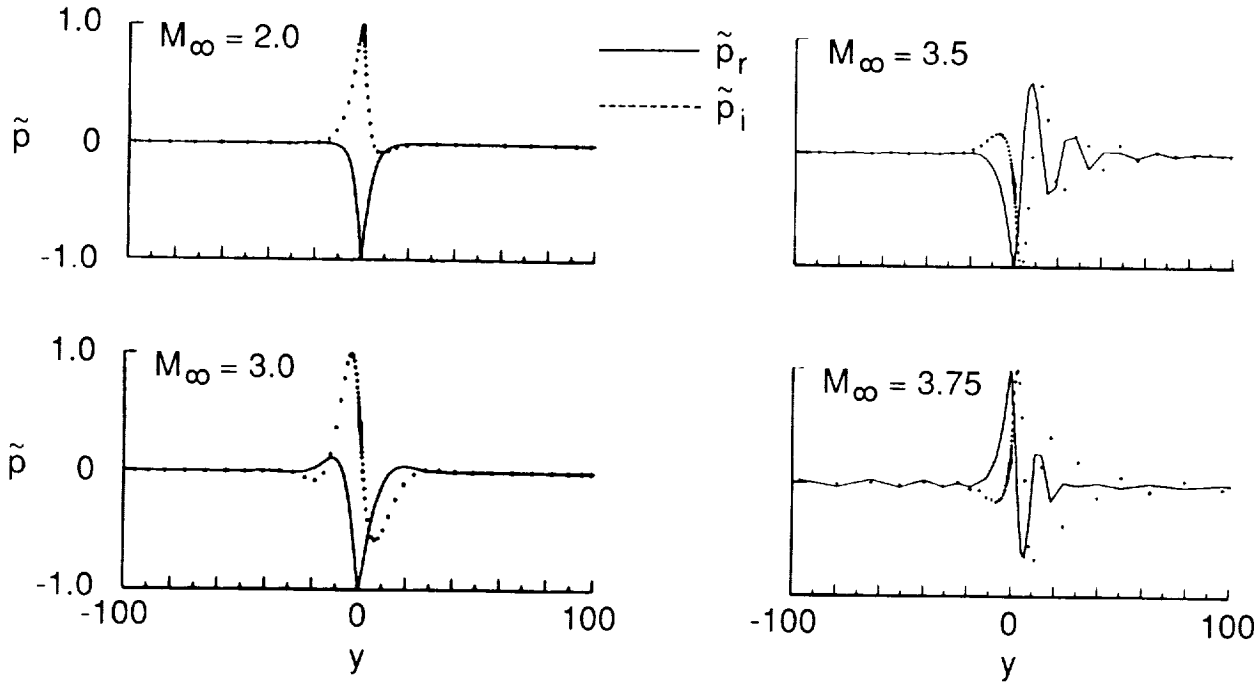

Figure 24. Pressure disturbance $\tilde{p}$ for increasing Mach number and with SDSPD in SPECLS. $\theta = 60°$.

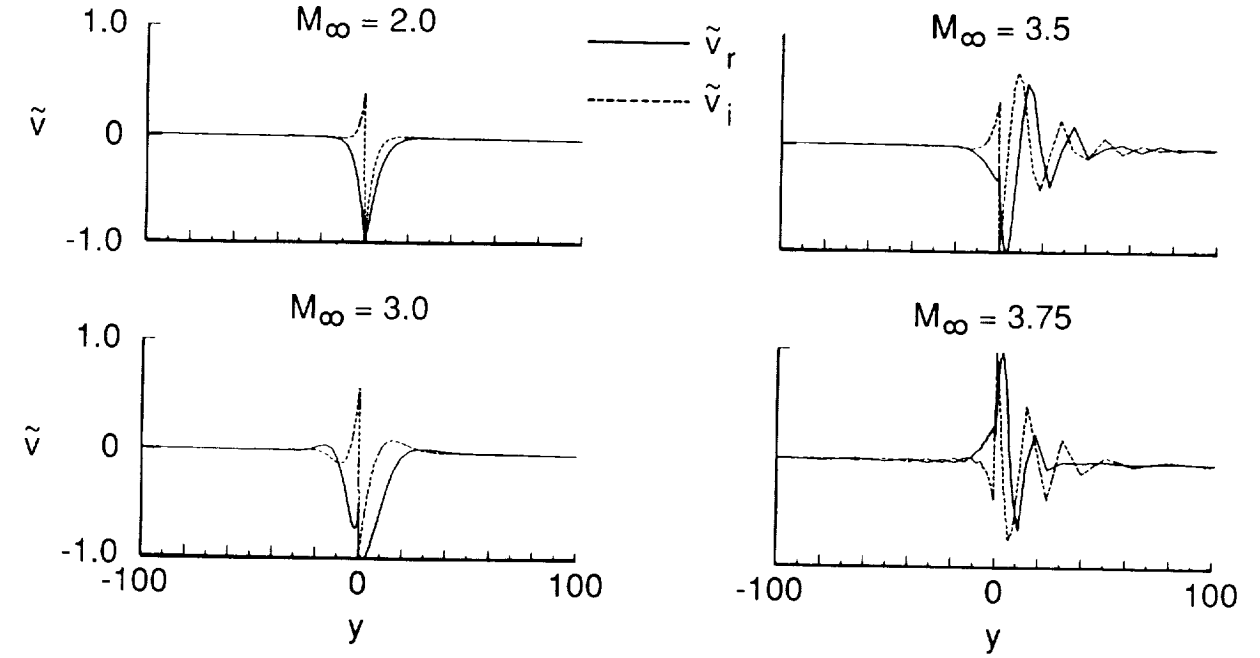

Figure 25. Normal-velocity disturbance $\tilde{v}$ for increasing Mach number and with SDSPD in SPECLS. $\theta = 60°$.

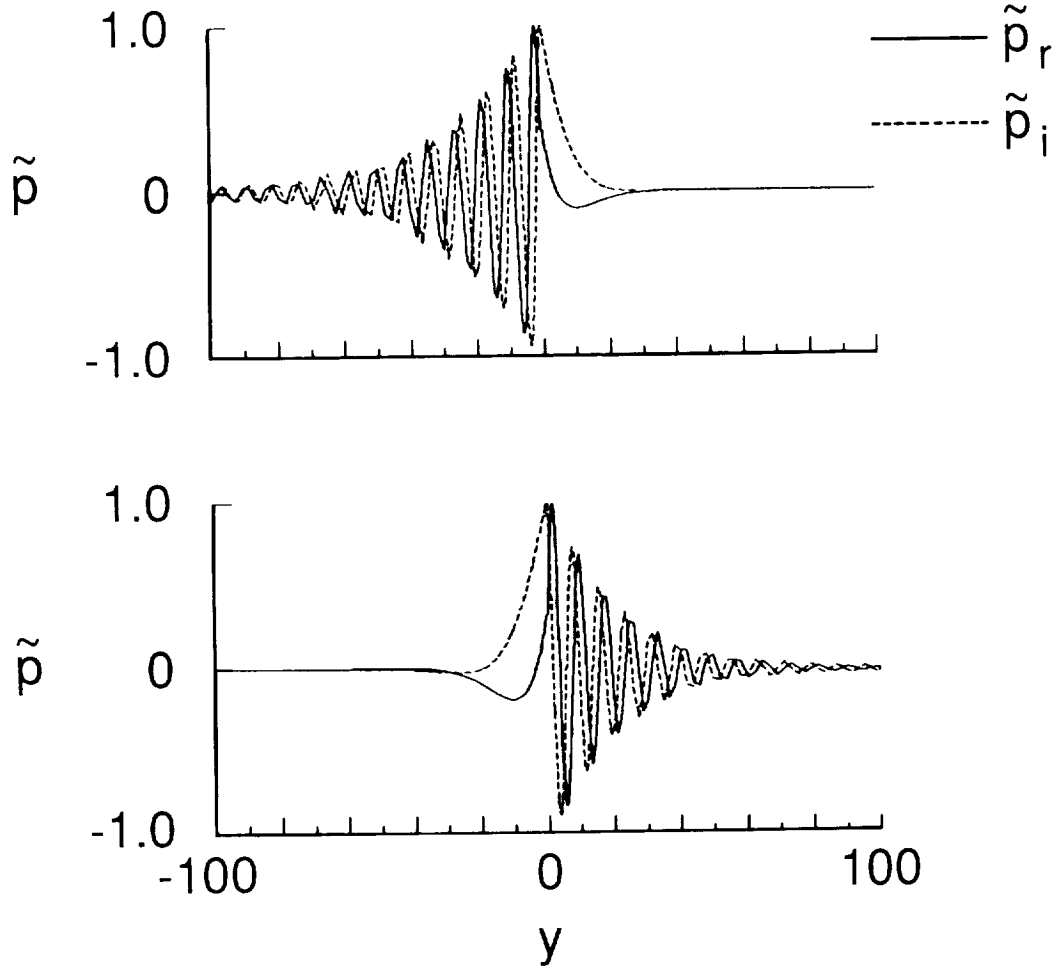

Figure 26. Pressure disturbance $\tilde{p}$ for two unstable supersonic modes obtained with MDSPD in SPECLS. $M_\infty = 4$; $\theta = 33.5°$. Discretization: center domain on [-1,1], 41 points; oscillatory side, 105 points; smooth side, 25 points.

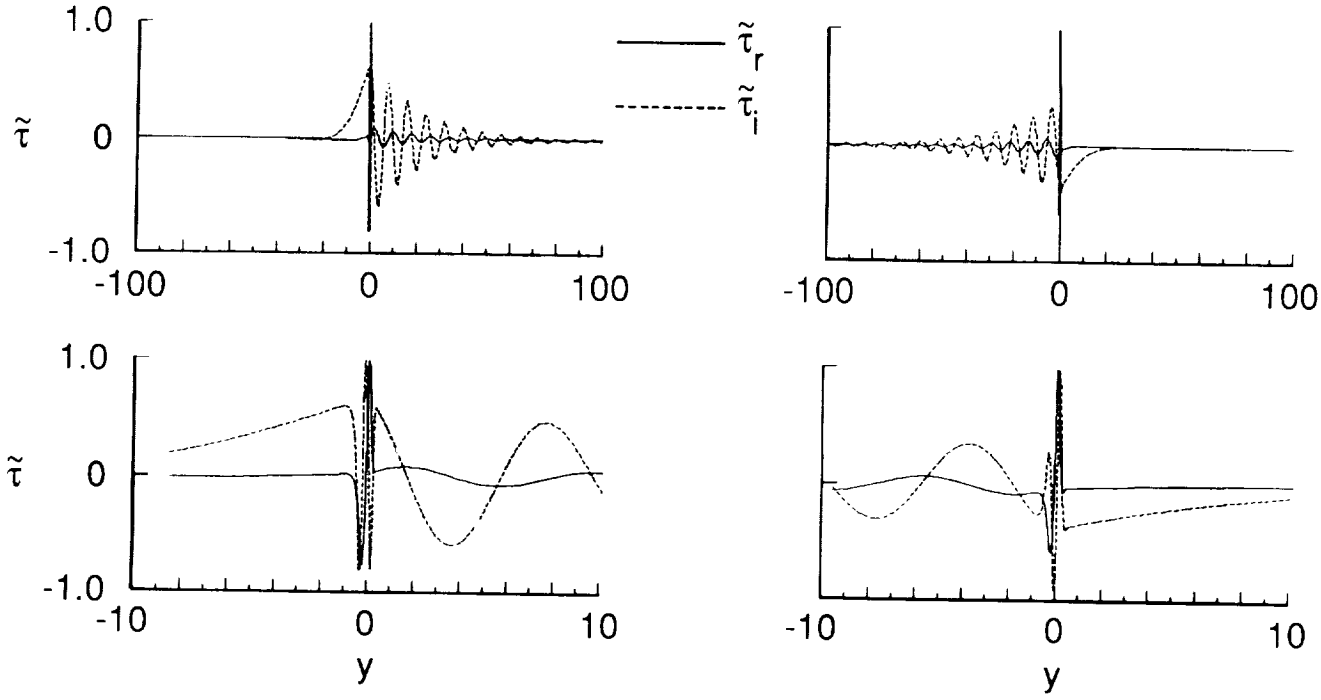

Figure 27. Temperature disturbance $\tilde{\tau}$ for two unstable supersonic modes of figure 26 plotted on full domain [−100,100] and expanded domain [−10,10].

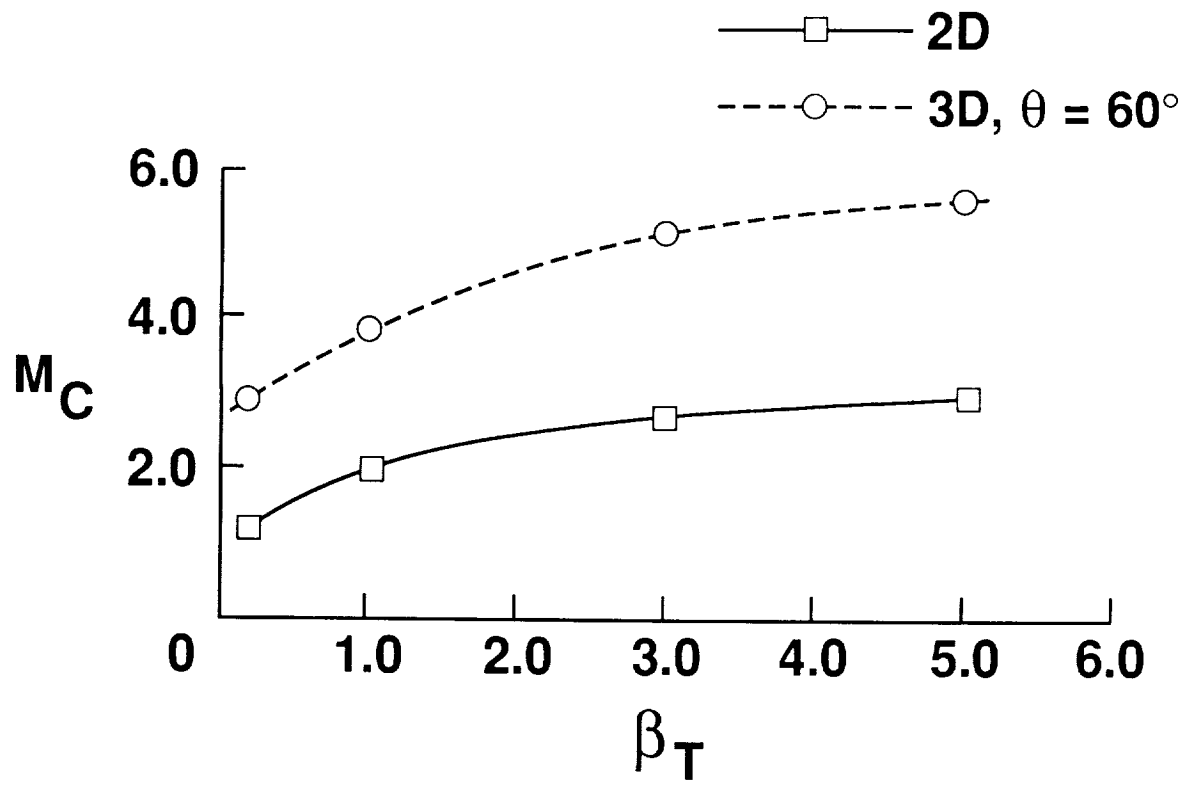

Figure 28. Critical Mach number versus β_T for two-dimensional (2D) and three-dimensional (3D) disturbances.

NASA
National Aeronautics and Space Administration

Report Documentation Page

1. Report No.	2. Government Accession No.	3. Recipient's Catalog No.
NASA TP-2858		

4. Title and Subtitle	5. Report Date
A Spectral Collocation Solution to the Compressible Stability Eigenvalue Problem	December 1988
	6. Performing Organization Code
7. Author(s)	8. Performing Organization Report No.
Michéle G. Macaraeg, Craig L. Streett, and M. Y. Hussaini	L-16470
9. Performing Organization Name and Address	10. Work Unit No.
NASA Langley Research Center Hampton, VA 23665-5225	505-60-01-02
	11. Contract or Grant No.
12. Sponsoring Agency Name and Address	13. Type of Report and Period Covered
National Aeronautics and Space Administration Washington, DC 20546-0001	Technical Paper
	14. Sponsoring Agency Code

15. Supplementary Notes

Michéle G. Macaraeg and Craig L. Streett: Langley Research Center, Hampton, Virginia.
M. Y. Hussaini: Institute for Computer Applications in Science and Engineering, Langley Research Center, Hampton, Virginia.

16. Abstract

A newly developed spectral compressible linear stability code (SPECLS) using a staggered pressure mesh for analysis of shear flow stability is presented and applied to high-speed boundary layers and free shear flows. The formulation is the first application of a staggered mesh for a compressible flow analysis by a spectral technique. For equivalent accuracy of growth rates, an order of magnitude fewer points are needed by SPECLS than by a finite difference formulation. Supersonic disturbances, which are found to have highly oscillatory structures, have been resolved by a spectral multi-domain discretization, which requires a factor of three fewer points than the single-domain spectral stability code. The study indicates, as expected, that stability of mixing layers is enhanced by viscosity and increasing Mach number. The mean flow involves a jet being injected into a quiescent gas. Higher temperatures of the injected gas also enhance stability characteristics of the free shear layer.

17. Key Words (Suggested by Authors(s))	18. Distribution Statement
Compressible shear layer Hydrodynamic stability Spectral methods	Unclassified—Unlimited Subject Category 02

19. Security Classif.(of this report)	20. Security Classif.(of this page)	21. No. of Pages	22. Price
Unclassified	Unclassified	41	A03

NASA FORM 1626 OCT 86 NASA-Langley, 1988
For sale by the National Technical Information Service, Springfield, Virginia 22161-2171

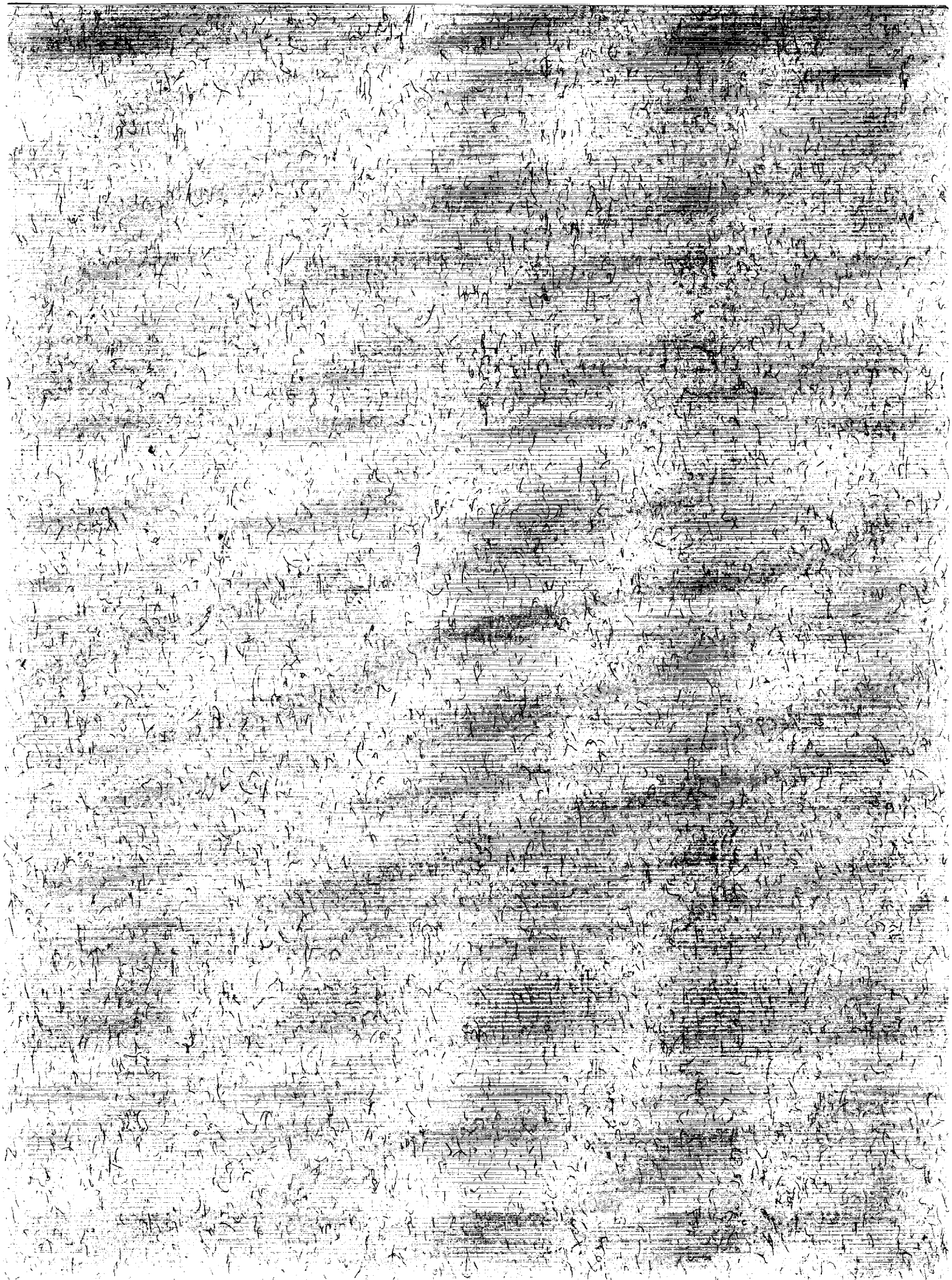

National Aeronautics and
Space Administration
Code NTT-4

Washington, D.C.
20546-0001